Gabbroic-dioritic dykes from the Sanadaj-Sirjan Zone, Zagros Orogen: windows on Jurassic and Eocene geodynamic processes in western Iran

Reza Deevsalar [1,*], Ryuichi Shinjo [2], Kuo-Lung Wang [3], Yeganehfar Hadi [4] & Iain Neill [5]

[1] *Department of Geology, Tarbiat Modares University, Tehran 14115-175, Iran.*

[2] *Department of Physics and Earth Sciences, University of the Ryukyus, Japan.*

[3] *Institute of Earth Sciences, Academia Sinica, Nankang, Taipei 115, Taiwan.*

[4] *Department of geology, Payame Noor University (PNU), Tehran 19395-3697, Iran*

[5] *School of Geographical and Earth Sciences, University of Glasgow, Glasgow G12 8QQ, Scotland.*

* Corresponding author. E-mail: deevsalar@gmail.com

Abbreviated Title: Arc to Within-Plate Magmatism, NW Iran

Supplementary material: Field photographs, photomicrographs, additional geochemical plots, descriptions of analytical methods and tables of geochemical modelling parameters are available at https://doi.org/xxxx.

Abstract: The Sanandaj-Sirjan Zone (SaSiZ) is a magmatic-metamorphic portion of the Zagros Orogen, western Iran, marking the Tethyan suture zone between the Afro-Arabian Plate and the Central Iran Micro-Continent. Mafic-intermediate dyke swarms with Middle Jurassic (Group-1: hornblende gabbro and diorite) and Late Eocene (Group-2: hornblende-pyroxene gabbro) ages are recognized in the Malayer-Boroujerd Plutonic Complex of the northern SaSiZ. Group-1 dykes have elemental and isotopic signatures consistent with melting of subduction-modified mantle which relates to Neo-Tethyan subduction processes. Some Group-1 magmas evolved to intermediate compositions through assimilation and fractional crystallization processes. Group-2 dykes have within-plate trace element geochemical signatures, modelled as deriving from low-degree melting of asthenospheric mantle without a subduction influence. Published models postulate either a Cretaceous-Eocene Neo-Tethyan flat-slab scenario, or a Latest Cretaceous-Palaeogene Neo-Tethyan break-off event beneath the SaSiZ. Such models do not reconcile with the Late Eocene presence of within-plate magmatism in westernmost Iran, very close to the Zagros Suture. We argue that a period of flat-slab subduction concluded with sub-parallel subduction of ridge to the trench and subsequent slab break-off in the Late Eocene, that is responsible for generation of the distinct Mesopotamia and Zagros slabs in mantle tomography models. Break-off was followed by small volume within-plate type magmatism before short-lived re-establishment of Tethyan subduction prior to the final Arabia-Eurasia collision.

-end abstract-

Mafic rocks exposed in convergent settings yield important information about subduction zone environments and magmatic evolution (e.g. Turner *et al.* 1997). In general, the mantle source for the continental arc systems is metasomatically enriched by fluids and/or melts derived from the subducting slab (Ellam & Hawkesworth 1988). Most subduction-related rocks therefore display distinctive geochemical characteristics such as elevated concentrations of light or mobile incompatible trace elements and relative depletions in high field strength elements (Pearce & Peate 1995). The lack of a subduction-related geochemical signature, in mantle-derived mafic rocks formed at or around the time of subduction, may indicate unusual chemical or geodynamic circumstances. These situations can be melting of enriched mantle pockets (Hastie *et al.* 2011), the presence of slab windows (Zandt & Humphreys 2008), slab tearing or break-off (Davies & von Blanckenburg 1995), all of which may allow the rise of melts derived from asthenospheric sources without the necessity for a slab-derived geochemical component. Unfortunately, in many continental arc settings, mafic rocks are at a premium, so hypotheses about igneous petrogenesis and the geodynamic conditions of past subduction events may be obscured by fractional crystallization and crustal contamination processes.

This paper is an extension of previous work (Deevsalar *et al.* 2017) on the mafic intrusive rocks from the Malayer-Boroujerd Plutonic Complex (MBPC) in the Sanandaj-Sirjan Zone (SaSiZ), W Iran, which concentrated mainly on mafic-intermediate plutonic rocks. The Mesozoic–Cenozoic SaSiZ (mainly plutonic) and the Cenozoic Urumieh-Dokhtar Magmatic Arc (UDMA) are two major magmatic terranes of the Zagros Orogen (Fig. 1a). The orogen, part of the Cenozoic Alpine-Himalayan mountain belt, is a consequence of Neo-Tethyan Ocean closure and the subsequent collision between the Central Iran Micro-Continent and the Afro-Arabian Plate (e.g. Stampfli & Borel 2002; Agard *et al.* 2011; Verdel *et al.* 2011; Mouthereau *et al.* 2012; Azizi *et al.* 2015). The SaSiZ is a metamorphic-magmatic terrane dominated by igneous rocks that occur mostly as plutons, stocks and irregular minor intrusions separated by metamorphic units. The subject of this present investigation, the MBPC, is in the northern SaSiZ (N-SaSiZ) and is spatially the closest magmatic complex to the Zagros Thrust Fault (Fig. 1a) at the present level of exposure. Successive magmatic events in the N-SaSiZ include: (1) Late Permian basaltic volcanic activity (Stampfli & Borel 2002), (2) Middle Jurassic to Early Cretaceous calc-alkaline Andean-type granites accompanied by dioritic and gabbroic intrusions (e.g. Ghalamghash 2003; Ghalamghash *et al*. 2009; Ahmadi-Khalaji *et al.* 2007; Sepahi 2008; Ahadnejad *et al.* 2010; Mahmoudi *et al.* 2011; Ghaffari *et al.* 2013; Azizi *et al.* 2015; Deevsalar *et al.* 2017); (3) Paleocene–Eocene gabbroic (Mazhari *et al.* 2009; Deevsalar *et al.* 2017) and granitic (Rashidnejad-Omran *et al.* 2002; Azizi & Moinevaziri 2009; Mahmoudi *et al.* 2011) intrusions. Magmatic activities in the MBPC occurred during phases (2) and (3) of magmatic activity in the N-SaSiZ. Here are very rare exposures of intrusive mafic rocks which formed during the subduction of the Neo-Tethys Ocean beneath the Central Iran Micro-Continent (Deevsalar *et al.*

2017). Following on from a study of gabbroic plutonic rocks within the MBPC (Deevsalar *et al.* 2017), here we focus on suites of mafic–intermediate dykes. They are of interest as they preserve less-evolved compositions which may be used to model the original mantle source of magmatism compared to more dominant contemporaneous felsic rocks. The dykes are also much less affected by the accumulation of crystal phases compared to contemporary plutonic facies.

The geochemical study is undertaken to provide constraint on the petrogenesis of two suites of mafic-intermediate dykes, one suite dating to the Middle Jurassic and one to the Late Eocene. In turn, we reflect on the respective geodynamic settings of the dykes. The Late Eocene suite will be emphasised, as it displays little evidence for interaction with subduction-related components and can thus be used to challenge existing geodynamic models for slab geometry during the onset of the Arabia-Eurasia collision (e.g. Agard *et al.* 2011; Verdel *et al.* 2011). The new geochronology, petrography, and elemental and isotopic geochemistry for the mafic-intermediate dykes will thus be employed to constrain the geochemical properties of the mantle source region(s), their magmatic evolution and implications for geodynamic models of the region.

The Malayer-Boroujerd Plutonic Complex (MBPC)

The MBPC comprises abundant irregularly-shaped exposures of igneous rocks that form a band striking NW−SE over an elongated area of some 1000 km^2 (Fig. 1b). The MBPC is surrounded by metamorphic units like much of the N-SaSiZ. The MBPC displays a wide spectrum of magmatic compositions, although these are dominantly felsic (Fig. 1b, geological map of the NW- and SE-MBPC entitled '8' and '9'). The MBPC felsic rocks range from syenogranite–monzogranite to granodiorite–tonalite, the granitoids being the dominant lithology especially in the south-eastern part of the MBPC. The MBPC granitoids intrude into the Jurassic Hamadan phyllite metamorphic assemblage with well-defined, sharp contacts. Magma emplacement generated contact metamorphic aureoles composed of andalusite, garnet and staurolite hornfels (Masoudi 1997). Intermediate units occur as dykes and enclaves within the felsic rocks and as larger mappable ‘patches’ (irregularly shaped intrusions) of diorites (Deevsalar *et al.* 2018). Mafic stocks, patches, dykes and veins form exposures of various sizes and they are often found at the margins of the larger felsic bodies (Deevsalar *et al.* 2014) (Supplementary Item 1, Fig. S1). Zircon U–Pb dating of the felsic rocks, which are intruded by the MBPC mafic-intermediate dykes, yielded ages of 162 to 187 Ma for the NW-MBPC (Ahadnejad *et al.* 2010) and 169 to 172 Ma for the SE-MBPC (Ahmadi-Khalaji *et al.* 2007).

Field and Petrographic observations

These MBPC dykes are 0.5–5 m wide and usually exposed for between 5 and 30 m along-strike, although lengths of up to 150 m have been observed. There are no preferred strike directions for the MBPC dykes for either of the geochemically distinct groups or from dykes with different ages (Supplementary Item 1, Fig. S1). They comprise samples with either a fine-grained aphyric or a porphyritic texture. The dykes are dark-grey to dark-green and range from hornblende-bearing pyroxene gabbros to diorites (after Streckeisen 1976). In the field, the dykes are predominantly hosted in granitoids and occasionally in metamorphic country rock, but those from different groups do not show any obvious difference in their locations relative to other igneous and metamorphic rocks. The larger porphyritic dykes have fine-grained chilled margins and smaller dykes are mainly fine-grained dolerites. The mineralogy of these two types based on outcrop size and inferred volume is similar, yet there are discernible texture and grain-size differences.

The dykes of different geochemical groups (discussed further in following sections) cannot be distinguished by difference in their constituent minerals, mineral modal proportion, alteration or texture. However, in general the mafic gabbroic dykes are of two kinds: (1) a porphyritic type composed of 20 – 40 vol. % medium–coarse-grained plagioclase phenocrysts (2 – 4 mm) and medium-grained clinopyroxene and amphibole (2 mm) in a 60 – 80 % groundmass of plagioclase, clinopyroxene, amphibole, opaque minerals (mainly hematite), chlorite and sericite, and (2) fine-grained doleritic dykes composed of microlitic or lath-like plagioclase grains with alignment and amphibole, clinopyroxene, secondary biotite and minor hematite and chlorite. In contrast, dioritic dykes have plagioclase (35 – 50 vol. %), alkali feldspar (0 – 10 vol. %), hornblende (15 – 40 vol. %), biotite (0 – 8 vol. %), pyroxene (0 – 5 vol. %), chlorite and epidote (0 - 5%) and minor phases including opaque minerals and apatite are <1 vol. % (Supplementary Item 1, Fig. S2).

Analytical results

Geochronology

Using zircon U–Pb geochronology, several studies of the SaSiZ have reported Middle-Upper Jurassic ages for the granitic rocks. As well as these results, two granitic intrusions from Marivan (NW-SaSiZ, area "5" in Fig. 1b) (~ 38 Ma, Sepahi *et al.* 2014) and Gosheh–Tavandasht (SE-MBPC, area "9" in Fig. 1b) (~ 34.9 Ma; Mahmoudi *et al.* 2011) demonstrate much younger magmatic activity. The presence of inherited Proterozoic-Paleozoic zircons in granitoids indicates that this part of the SaSiZ is underlain by much older crystalline basement (Ahadnejad *et al.* 2010). The age of the mafic rocks from the SaSiZ have been poorly constrained thus far. Mazhari *et al.* (2011) gave an age of 96 ± 2 Ma for the Naqadeh gabbro–dioritic rocks (Fig. 1b, area "2" (N-K-P)) and Mahmoudi *et al.* (2011) reported ages of 149.5 and 164 Ma for Qorveh gabbroic (Fig. 1b, area "4" (Qr)) and Alvand dioritic rocks (Fig. 1b, area "7" (Al)). The recently constrained zircon U–Pb ages for the MBPC gabbroic intrusions yielded two distinct episodes of mafic magmatism in this area including Middle Jurassic and Late Eocene ages. The result indicates the co-occurrence of m afic, felsic and intermediate magmatism during Middle Jurassic and bimodal mafic-intermediate magmatism during Late Eocene of the MBPC.

For this study, three representative samples of gabbroic dykes (from NW-MBPC: MN_{2a}, M_{29} and M_{50}) and one dioritic dyke (from SE-MBPC: BR_{02}) from two geochemically distinct groups (see the next section) were chosen for U-Pb zircon dating by laser ablation inductively coupled plasma mass spectrometry (LA-ICP-MS). Analytical methods and procedures are fully presented in Supplementary Item 2, section A. Given that precise age measurements using $^{207}Pb/^{235}U$ and $^{207}Pb/^{206}Pb$ ratios are feasible usually only for Precambrian zircons (cf. Ireland & Williams 2003), the weighted mean of pooled $^{206}Pb/^{238}U$ ages are taken to indicate the crystallization ages of the samples in this study. Zircon U–Pb ages for 90 analytical points on individual zircon grains are given in Supplementary Item 3, Table S1. The separated zircons are mostly transparent, colourless to slightly brown and show oscillatory zoning (Fig. 2), indicative of a magmatic origin (Hoskin & Schaltegger 2003). The results of the LA-ICP-MS analyses for twenty-four points from sample MN_{2a} yielded weighted mean age of 169.8 ± 2 Ma (Supplementary Item 3, Table S1; Fig. 2a, and Fig. 3a). Forty-six grains from sample BR_{02} yielded a mean $^{206}Pb/^{238}U$ age of 166.93 ± 0.72 Ma (1σ) for zircon crystallisation (Supplementary Item 3, Table S1; Fig. 2b, and Fig. 3b), after rejecting three scattered or discordant ages (spots 6, 10 and 19) and one anomalous age likely due to large analytical uncertainties (spot 9). Of 9 points for sample M_{50}, 8 points give weighted mean age of 47.1 ± 0.7 Ma (Supplementary Item 3, Table S1; Fig. 2c, and Fig. 3c) and one point produced anomalous age likely indicating zircon inheritance (inherited zircon age of 1868 ± 18 Ma, spot 9). The 16 points analysed in sample M_{29} provide a concordant age of 36.1 ± 0.9 (Supplementary Item 3, Table S1; Fig. 2d, and Fig. 3d).

The presence of inherited zircons with a Mesoproterozoic age, like those detected in MBPC granitoids (e.g. Ahadnejad *et al.* 2010), indicates the presence of a crustal contaminant either as old crustal wall-rock or an old crystalline basement. The Middle Jurassic ages for gabbro-dioritic dykes are consistent with zircon U–Pb ages of subduction-related gabbroic intrusions from the MBPC (Deevsalar *et al.* 2017) and granitic rocks throughout the SaSiZ (e.g. Ahmadi-Khalaji *et al.* 2007; Ahadnejad *et al.* 2010; Shahbazi *et al.* 2010; Mahmoudi *et al.* 2011; Chiu *et al.* 2013; Sepahi 2014) and implies that syn-plutonic mafic-intermediate magmatism closely related in time and space to felsic magmatic activity. The geodynamic implications of Late Eocene gabbroic dykes (~42 Ma) and intrusive rocks (~40 Ma, Deevsalar *et al.* 2017) within the MBPC will be discussed later.

Major element geochemistry

The MBPC dykes have retained much of their original igneous texture; however, they experienced some sub-solidus weathering and low-grade metamorphism including growth of chlorite and epidote. Following careful sampling, the analysed MBPC dykes have chemical index of alteration values (= molecular $[Al_2O_3/(Al_2O_3+CaO+Na_2O+K_2O)] \times 100$, suggested by Nesbitt & Young 1982) lower than 50 (except of BR_{02} and M_{23}) as suggested for un-weathered igneous rocks (Ramkumar 2015). These dykes yielded low loss-on-ignition (LOI) values (mostly < 3 wt. %, except of M_{23}, BR_{02}, M_{29} and MN_{12}) indicating a modest extent of hydrothermal alteration. Low-grade metamorphism in these rocks might mobilize major and large ion lithophile elements (LILE) such as Ba and Rb (e.g. Floyd & Winchester 1975; Hastie *et al.* 2007). However, having recognized coherent primitive mantle- and chondrite-normalized patterns (Fig. 5), widespread remobilisation during metamorphism is unlikely. The consistency of trends observed in Figs. 4 and 5, for unaltered samples (low LOI) and those with slightly altered samples suggest that the concentrations of these elements were not selectively modified. Whole-rock major and trace element data for the MBPC mafic–intermediate dykes are given in Table 1. Analytical methods and procedures are presented in Supplementary Item 2, section B.

As given earlier, based upon geochemical characteristics, two set of dyes have been identified in the MBPC. The first group of MBPC dykes comprise mafic gabbros (n = 3, samples MN_{08} and BR_{03b} and MN_{2a}) and intermediate samples with dioritic compositions (n = 3, samples M_{23}, BR_{07} and BR_{02}) (Table 1). Whole-rock SiO_2 in these samples varies from ~45 to 62 wt. % (Table 1). Graphs of whole-rock oxides vs. SiO_2 (Fig. 4a-f) show systematic variation in this group. The concentration of CaO, TiO_2, FeO_T, MgO and MnO decrease with increasing SiO_2 whereas Al_2O_3 and total alkalis (Na_2O + K_2O) increase. These dykes show a sub-alkaline character on a TAS plot (Fig. 4a). U-Pb dating of two selected samples from this group defines a Middle Jurassic age. We herein refer to the Middle Jurassic dykes as *Group-1*. In contrast to their coeval calc-alkaline gabbroic intrusions (Deevsalar *et al.* 2017), most of the dykes fall in tholeiitic fields on FeO^T/MgO vs. SiO_2 and AFM diagrams (Supplementary Item 1, Fig. S3). The dykes have also a wider range of TiO_2 (0.49 to 3.70) than contemporaneous Middle Jurassic gabbroic intrusions (0.29 to 0.64) (Deevsalar *et al.* 2017).

The next group of MBPC dykes have gabbroic compositions (n= 16, Table 1). The SiO_2 concentrations of Group-2 dykes display a small range (~47 to 49 wt. %, Table 1). They have relatively small range of MgO (~5 to 7 wt. %) in comparison to Group-1 dykes which range from 2 to 10 wt. % MgO. In Harker-style plots (Fig. 4a-f), major oxides or elements show correlation with SiO_2 despite the narrow SiO_2 range. SiO_2 positively correlates with CaO and Al_2O_3, and negatively correlates with MnO, FeO^T and TiO_2. MgO either does not correlate or the correlation is slightly positive with increasing SiO_2. U-Pb dating of two samples from this group is yielded Late Eocene ages. The Late Eocene mafic dykes are herein referred to as *Group-2*. The Group-2 dykes have an alkaline affinity on the TAS diagram (Fig. 4a), akin to their coeval gabbroic intrusions (Deevsalar *et al.* 2017) and contrasting with Group-1 dykes. TiO_2 content in Late Eocene gabbroic dykes varies within a small range (1.9 to 3.8 wt. %) compared to those coeval gabbroic intrusions (1.9 to 5.5 wt. %; Deevsalar *et al.* 2017).

Trace element geochemistry

The MBPC dykes of different ages can be clearly distinguished in terms of trace element characteristics. Group-1 dykes have high Sr (~300 to 600 ppm), while those from Group-2 have lower Sr concentrations (~50 to 100 ppm). Group-1 dykes display systematic variations in relative modal abundances of Fe-Ti oxides, including ilmenite and rutile, which reflect in their vanadium concentrations. The Group-1 dykes are characterised by distinctive enrichments in LILE and light rare earth elements (LREE), and by depletion of high field strength elements (HFSE) and heavy rare earth elements (HREE), especially in those of dioritic character (Fig. 5a). The diorites have the highest LILE (La, Ba and Rb) and Th concentrations. The primitive mantle-normalized trace element diagrams show negative anomalies for Nb, Ta and significant depletion in Sr (Fig. 5a), akin to the Middle Jurassic non-cumulate gabbroic plutonic rocks also found in the MBPC (Deevsalar *et al.* 2017). Aside from the distinctive negative HFSE and Sr anomalies, sample MN_{2a} shows slightly negative Ti and Zr anomalies (Fig. 5a). The total REE concentration (∑REE) in Group-1 dykes varies from 123 to 204 ppm. These Jurassic rocks display LREE-enriched and HREE-depleted chondrite-normalised (CN) patterns (Fig. 5b), including negative Eu anomalies (Eu/Eu^*_{CN} = 0.61 to 0.69), as well as relatively high $(La/Yb)_{CN}$ of 5 to 15 (Table 1). In comparison, the contemporaneous Middle Jurassic non-cumulate gabbroic intrusions are enriched in LREE and have less variable LREE/HREE fractionation (Deevsalar *et al.* 2017).

The Group-2 gabbroic dykes are characterised by slight and variable enrichment in the LILE relative to the LREE and HFSE (Fig. 5c). The dykes also show variable degrees of LREE/HREE fractionation with La/Yb_{CN} ranging from 4-10 (Fig. 5d). Group-2 dykes contain slightly negative to positive Eu anomalies with Eu/Eu*= 0.93–1.31 (Fig. 5d) and lower ∑REE (94 to 152 ppm) than the

Group-1 dykes. The Group-2 dykes have primitive mantle-normalized and chondrite-normalized REE patterns consistent with their alkaline affinity and show a typical within-plate character (Winchester & Floyd 1977). There is no significant depletion in HFSE such as Nb, Ta, Zr, Hf and Ti (Fig. 5c), which is remarkably consistent with within-plate rocks from modern ocean islands.

Radiogenic isotopes

Whole-rock Sr, Nd and Pb isotopic compositions of representative samples of mafic–intermediate dykes from the MBPC are shown in Tables 2 and 3. Analytical methods and procedures are presented in Supplementary Item 2, section C. Initial values for the $^{87}Sr/^{86}Sr$ and $^{143}Nd/^{144}Nd$ ratios are calculated at 168 Ma for Group-1 and at 42 Ma for Group-2 dykes. On Figure 6, the isotopic composition of the MBPC samples are plotted against mafic rocks derived from different mantle sources beneath the modern Turkish–Iranian Plateau (Supplementary Item 3, Table S2).

The Group-1 dykes display wide range variations of $(^{87}Sr/^{86}Sr)_i$ ratios albeit at uniform εNd_i ranging from 0.7077 to 0.7151 and -5.85 to -7.89, respectively. Initial $^{87}Sr/^{86}Sr$ ratios in this group are higher than those in Middle Jurassic calc-alkaline gabbroic intrusions from the MBPC, which had values ranging from 0.7035 to 0.70594 (Deevsalar *et al.* 2017). On Figure 6a, the Group-1 dykes plot parallel with the $^{87}Sr/^{86}Sr$ axis, extending from the mantle array to higher $(^{87}Sr/^{86}Sr)_i$ ratios. All the samples, except MN_{2a}, therefore plot outside of mantle array on Figure 6a. $(^{87}Sr/^{86}Sr)_i$ ratios of the two gabbroic dykes are broadly similar to that of dioritic dykes, indicating that these rocks may be linked through similar process on a common source. The Pb isotopic ratios are presented in Table 4 and plotted on Fig. 6b-e. The Pb isotope ratios of the gabbro-dioritic dykes from Group-1 are close to Cenozoic and Mesozoic magmatic rocks from a variety of tectonic settings across the modern Turkish-Iranian Plateau. In summary, this group exhibits moderately radiogenic Sr and Pb and unradiogenic Nd isotopic ratios.

The Late Eocene Group-2 samples have relatively lower Rb and higher Sr concentrations compared to Group-1 dykes, resulting in lower $^{87}Sr/^{86}Sr$ ratios. This group has comparatively uniform $(^{87}Sr/^{86}Sr)_i$ values and εNd_i, 0.7049 to 0.7074 and +0.76 to +3.29 respectively, roughly overlapping the values of Late Eocene alkaline gabbroic intrusive rocks from the MBPC (Deevsalar *et al.* 2017). In $^{87}Sr/^{86}Sr$ vs. εNd_i space, Group-2 dykes are less scattered that Group-1. Some samples plot within the mantle array (Fig. 6a). In comparison with mid-ocean ridge basalts and Hawaiian alkali basalts, at comparable $(^{87}Sr/^{86}Sr)_i$ ratios the Late Eocene dykes have lower εNd_i values (Fig. 6a). Group-2 dykes show only slightly higher $(^{206}Pb/^{204}Pb)_i$ and $(^{208}Pb/^{204}Pb)_i$ than Group-1 and similar $(^{207}Pb/^{204}Pb)_i$ (Fig. 6b-e).

Discussion

Crustal contamination

It is essential to evaluate if magmas have undergone crustal contamination before speculating on their source region. Unlike the nearby felsic plutonic bodies, the MBPC gabbro-dioritic dykes do not record macroscopic evidence for crustal assimilation such as metamorphic xenoliths or refractory metamorphic minerals. Therefore, closer inspection of elemental and isotopic data is required. High SiO_2 and alkalis and low MgO, which are expected in substantially contaminated magmas (e.g., Jahn *et al.* 1999; Zhang *et al.* 2002), were only observed in Group-1 diorites. There is minimal evidence of zircon inheritance (one inherited zircon in MN_{2a}, Supplementary Item 3, Table S1) during Middle Jurassic dyke emplacement, although it is entirely possible that inheritance was not picked up due to potential for biased recovery during preparation of zircon separates, or dissolution of zircon within the mafic host. Sample MN_{2a}, despite the recorded zircon inheritance, is the only analysed Group-1 sample to fall within the mantle array on Figure 6a. The remaining Group-1 dykes form a parallel array towards higher $^{87}Sr/^{86}Sr$ and thus upper continental crust composition (Fig. 6a). This evidence is compounded by the overall arc-like elemental signatures of the Group-1 samples, and the fact that contemporary Middle Jurassic mafic plutonic rocks almost all sit within the mantle array (Deevsalar *et al.* 2017). It seems that sample MN_{2a} would be the best choice for further modelling of the mantle source from the dyke suite.

In the Group-2 gabbro dykes, there is also little evidence for zircon inheritance (one inherited zircon in M_{50}, Supplementary Item 3, Table S1). There is an obvious lack of typical crustal trace element signatures (i.e. there is no high LILE/HFSE signature) in most of the samples. High $(^{87}Sr/^{86}Sr)_i$ (~ 0.707) in three of the samples (M_{33}, M_{38} and M_{50}; Fig. 6a) could be related to crustal contamination, however the trend shown on Figure 6a is parallel to the y-axis and could be related to later fluid-related alteration. There is no systematic LILE variation in these samples relative to those within the mantle array which further suggests only limited crustal contamination. These high-$(^{87}Sr/^{86}Sr)_i$ samples will nevertheless be excluded from further discussion. The general lack of crustal signatures in Group-2 remains consistent with a within-plate character, and is discussed further below.

Fractional crystallisation (FC)

The generation of low-MgO, high-alumina rocks by fractional crystallization of high-MgO primary mafic magma is typical of magmatic arc settings (Bartels *et al.* 1991; Draper & Johnston 1992). The Group-1 dykes contain wide ranges of MgO, Cr, Ni and Co (Table 1), implying they experienced varying degrees of fractional crystallisation (FC). The range in MgO values (from 10 to 2 wt. %) correlate with the wide range of Cr (83.7-904 ppm) and Ni (44.8-273.1 ppm) abundances. The samples do not contain sufficiently high MgO to indicate the presence of near-primary compositions. In Group-1 dykes, sample MN_{2a} with highest Mg# number ($Mg^{\#} = Mg^{+2}/(Mg^{+2}+Fe^{+2})$: 0.57) and high Cr and Ni concentrations, is representative of the least differentiated magma. A systematic change in total REE concentration (∑REE) is expected for magmas which undergo fractionation of phases in which the REE are incompatible. This feature is observed for Group-1, where ∑REE positively correlate with SiO_2 (inset plot, Supplementary Item 1, Fig. S4a). These dykes also have negative Eu anomalies (Fig. 5b) and low Sr concentrations (Table 1), which are likely due to fractional crystallization of plagioclase or presence of plagioclase in the source rocks (e.g. Hanson 1978). There are also systematic variations of SiO_2 and MgO with major oxides and trace elements in Harker diagrams (see Fig. 4a). Increasing Al_2O_3 contents and decreasing CaO/Al_2O_3 ratios with decreasing MgO contents (Fig. 4b) accompanied with decreasing Cr and V contents with increasing Zr concentrations (Supplementary Item 1, Fig. S4a, b, c) indicate fractionation of clinopyroxene. In general, the trends exhibited by the major oxides (Fig. 4a) can be explained in terms of fractionation of plagioclase, clinopyroxene along with apatite and accumulation of Fe-Ti oxides.

The Group-2 gabbroic dykes exhibit only a small range of SiO_2 (47 to 49 wt. %) and MgO (5 to 7 wt. %), and low Ni, Co, Cr and V (Table 1), so these dykes are unlikely to represent primary mantle melts. As shown in Supplementary Item 1, Fig. S4a to S4f, general trends on Harker-style diagrams are consistent with the fractionation of olivine and clinopyroxene or chrome-spinel. The fractionation of Fe-Ti oxides is supported by a negative trend observed on the FeO^T vs. SiO_2 graph (Fig. 4b) and the positive trend on a TiO_2 vs. MgO graph (Fig. 4i). The slightly positive Eu anomaly in this group rules out plagioclase fractionation.

Mantle source characteristics

The presence of Middle Jurassic gabbroic plutonic rocks in the MBPC, with only slightly less isotopically enriched signatures to MN_{2a}, also lends credence to using MN_{2a} to at least qualitatively discuss the Middle Jurassic mantle source. These rocks are characterized by enrichment in LILE and depletion of HFSE with all the distinctive features of continental subduction zone setting. The significant negative anomaly for Nb and Ta in all the Middle Jurassic dykes (Fig. 5a) indicates the influence of a relatively Nb-Ta depleted aqueous fluid derived from oceanic sediments as opposed to the influence of a silicate melt in which Nb and Ta have high solubility (Ionov & Hofmann 1995). Furthermore, the position of Group-1 dykes in Th/La vs. $(Ce/Ce^*)_{Nd}$ plot (Hastie *et al.* 2013; Supplementary Item 1, Fig. S5), including that of MN_{2a}, suggest that the source region was contaminated with sedimentary components equivalent to continental detritus/GLOSS II. This is consistent with geological evidence for Tethyan subduction on the Eurasian margin throughout the Mesozoic and Paleogene (Dilek & Sandvol 2009; Agard *et al.* 2011; Verdel *et al.* 2011; Chiu *et al.* 2013). Furthermore, the isotopically enriched Sr-Nd-Pb signatures of even the least contaminated samples, suggest partial melting of metasomatised mantle was probably a major contributor to their petrogenesis, like the coeval gabbroic intrusions. However, the slightly lower εNd_i values in Middle Jurassic gabbro-dioritic dykes compared to gabbroic plutonic rocks seem to indicate a higher volume of subducted materials (or greater extents of contamination) were involved in the genesis of the former.

For the Group-2 Late Eocene gabbro dykes, the narrow range of SiO_2, MgO > 4 wt. %, high TiO_2 and low La/Nb ratios (OIB-like signatures), as well as high concentrations of typical basaltic components (i.e. $Al_2O_3 \approx 14$ to 18 wt. %, $FeO^T \approx 10$ to 12 wt. %, and CaO ≈ 9 to 11 wt. %) reflect a fertile mantle source. As the ratios of non-mobile elements, including Nb, Ta, Zr and Hf are not usually affected by aqueous fluids and remain constant during magmatic processes, they can be used to investigate the original composition of the mantle source (Pearce & Peate 1995). As a result of their variable Hf/Yb and relatively constant Nb/Zr ratios, the Group-2 dykes plot within the enriched mantle field (EM-type) in Fig. 7a (John *et al*. 2004). In Th/Yb vs. Ta/Yb space they plot within the mantle array and show within-plate affinity (Fig. 7b). The enriched mantle source for

Group-2 is further highlighted on Figure 7c, where samples plot close to the OIB compositional field and above Western Anatolian Mantle compositions (WAM; Aldanmaz *et al.* 2000), E- and N-MORB (Enriched and Normal Mid Oceanic Ridge Basalt). However, on Supplementary Item 1, Fig. S5, the Group-2 dykes sit above the N-MORB field. An OIB-like signature is also supported by Zr/Ta vs. Nb/Hf variations (Fig. 7d) and the primitive mantle normalized multi-element diagram (Fig. 7e), in which Group-2 dykes show OIB-type trajectories. A lack of HFSE depletion, minor enrichment of LILE and LREE and no significant Eu anomalies (Fig. 5d), indicate these are within-plate rocks originating either from the asthenosphere (Sun & McDonough 1989; Wittke & Mack 1993), or an enriched upper mantle source (e.g. Hastie *et al.* 2011) without contemporary subduction influence. However, the trace element composition may necessitate incorporation of enriched mantle in the genesis of group-2 dykes (e.g., Lassiter *et al.* 2000; Lundstrom *et al.* 2003), but given the depleted isotopic signatures, these are most likely small-batch melts formed by low degree melting of depleted upper mantle asthenosphere (e.g., Ramos & Key, 1992; Gorring *et al.* 1997). This outcome is more consistent with the rare and small outcrops of Late Eocene exposed mafic rocks (in both forms of dykes and intrusions) within the MBPC.

Mantle melting process

The occurrence of less fractionated samples with near primary melt composition among the samples from Group-1 and Group-2 indicates melting of mantle lithologies. It may still be possible to model the extent of partial melting responsible for the generation of the least-evolved samples. As postulated by Jaques & Green (1980), the composition of primary mafic magma produced by melting of given source region under certain P-T conditions, is in part controlled not just by pressure and temperature, but by specific modal mineralogy. For the MBPC, the conditions of partial melting almost certainly will have changed between the subduction-related magmatism of the Middle Jurassic to the within-plate setting of the Late Eocene, concurrent with the models for contemporary gabbroic intrusions (Deevsalar *et al.* 2017).

Because of different phase/melt partition coefficients of Yb and Gd for garnet and spinel (McKenzie and O'Nions, 1991), a mantle source with residual spinel will produce $(Gd/Yb)_{CN}$ ratios ~ 1.2, whereas those melts originated from garnet-bearing source are expected to have higher values (Allen *et al.* 2013; Kelemen *et al.* 2003). The, $(Gd/Yb)_{CN}$ ratio (MN_{2a}), least fractionated sample from Group-1, is 1.49., However, $(Dy/Yb)_{CN}$ ratio of this sample (= 1.9) is in the range of values suggested for garnet-spinel (~ 1.5) and garnet-bearing mantle sources (> 2.5) (e.g. Chang *et al.* 2009; Jiang *et al.* 2010). This observation may indicate a changing depth of melting within the garnet-spinel transition zone, which is consistent with the result for contemporary gabbroic intrusions. Given the high Ba/Rb ratio in MN_{2a} (= 3.91), amphibole is also likely to have been present as a residual phase of melting mantle (Allen *et al.* 2013). Other possible processes include mixing between melts originated from garnet-bearing and spinel-bearing peridotites, which will be further examined using trace element models.

Melting, Mixing, FC and AFC models

To constrain the formation conditions of the Group-1 dykes, we modelled non-modal batch melting (Shaw 1970) of an assumed source, i.e. metasomatically enriched mantle lherzolite from the garnet-spinel transition zone, including maxima of 2 % amphibole, 7 % garnet and 3 % spinel (the parameters used in models and the results are given in Supplementary Item 3, Table S3, S4, Mode-I). The result for Mode-I indicates that 15 % partial melting of such a composition gives a best fit trajectory on primitive mantle-normalized trace element patterns of Group-1 dykes (Fig.8b; Table 4), consistent with the tholeiitic affinity of the Group-1 dykes (Jaques & Green 1980).

As already discussed, the closed-system fractional crystallization cannot be the only process involved in the magmatic evolution of Group-1 dykes, owing to the isotopic evidence for crustal contamination. The possible mechanism is open-system fractional crystallization plus assimilation of crustal materials either through AFC processes in shallow crustal magma chambers or mixing with crustal-derived melt. However, lower compatible element concentrations (such as Cr, Ni, Co) and higher $(^{87}Sr/^{86}Sr)_i$ ratios in dioritic dykes than those in the most primitive gabbroic sample (MN_{2a}) indicate a possible role for AFC-process in Group-1 dykes, but this is not supported by the results of trace element modelling of AFC (Figs. 8a, c). Alternatively, simple binary mixing model and multi-element modelling favours a two-component mixing process between mafic magma and felsic crustal melts. The results are shown as trajectories on $(^{87}Sr/^{86}Sr)_i$ vs. 1/Sr (Fig. 8b) and PM-normalized multi-element plot (Fig. 8d) (the parameters used in models and the results are given in Table 4 and Supplementary Item 3, Tables S2 to S4). Subsequent ascent will involve further cooling and fractional crystallization of these crustally-contaminated mafic magmas to produce the final Group-1 chemical composition (Fig. 8d).

For Group-2 dykes, the geochemical data attest of an origin by extraction of small melt batches from the asthenosphere, again within the garnet-spinel transition zone. In Fig. 9a, the melting model of an enriched mantle source — similar to Western Anatolian Mantle (WAM) — with garnet-spinel mineralogy (point M) for the MBPC Late Eocene Gabbros (Deevsalar *et al.* 2017) has been compared to that of depleted mantle with garnet-lherzolite and spinel-lherzolite compositions (point M′). However, melting trajectories of garnet-lherzolite and spinel-lherzolite sources on a La/Sm vs. La plot (Fig. 9a) are almost the same, but suggest they can be considered as the potential sources of magmatism. The La/Yb vs. Zr/Nb plot (Fig. 9b) indicate that the Group-2 dykes can be modelled by mixing of magmas generated by low degree melting of depleted mantle with garnet- and spinel-lherzolite mineralogy rather than enriched mantle. The geochemical models also suggest a more depleted composition of the asthenospheric source (M′ in Fig. 9a, b) than PM, but somewhat more enriched than N-MORB.Trace element modelling of non-modal batch melting (Table 5) demonstrates that small batch melts of garnet lherzolite source ($F_{melting}$ = 0.05, Mode-III; Supplementary Item 3, Table S3, S4), probably mixed with melts originated from spinel lherzolite in a shallower depth of mantle ($F_{melting}$ = 0.15, Mode-IV; Supplementary Item 3, Table S3, S4; F_{mixing} = 0.6). This model could explain the trends for the Group-2 dykes after the effects of FC are included (F_c: 0.45). Similar scenarios are frequently documented in the literature for the mafic alkaline rocks (e.g., Jaques & Green 1980; DePaolo & Daley 2000; Macpherson *et al.* 2006). The FC model conducted for the magmas indicates ~45 % fractional crystallisation of 0.5 Ol + 0.35 Cpx + 0.1 Am ± 0.05 Apt could explain the geochemical variations observed in the Group-2 dykes (Fig. 9c).

Implications for regional geodynamic models

As discussed above, the geochemical and isotopic characteristics of Middle Jurassic and Late Eocene gabbro-dioritic dykes from the MBPC imply changing magma sources. Such changes are likely to be associated with changing subduction dynamics, related to Tethyan ocean closure and the eventual onset of the wider Arabia-Eurasia collision. Such dynamics might include the rate, angle, depth and continuity of the subduction, all of which will control the location and chemistry of magmatic activity. We have little comment to pass on the Middle Jurassic Group-1 dykes: they formed at a time when there is unequivocal evidence for subduction of Neo-Tethyan oceanic crust beneath the Central Iran Micro-Continent.

Three key observations are relevant in discussion of the geodynamic situation in Iran during the Late Cretaceous to Eocene. 1) Termination of typical subduction-related magmatism prior to the end of Eocene is consistent with the within-plate character of the MBPC gabbroic intrusions (~ 40 Ma, Deevsalar *et al.* 2017) and confirms other recent studies of Eocene rocks in the UDMA (e.g.

Ballato *et al.* 2011; Verdel *et al.* 2011). Recently, Zhang *et al.* (in press) also described ~40 Myr old within-plate type rocks around Piranshahr around 500 km NW of Boroujerd (area "3" in Fig. 1b), the only other recorded Eocene magmatic rocks within the SaSiZ. 2) Separately, Agard *et al.* (2011) and Angiboust *et al*. (2016) tied exhumation of high pressure rocks in the Zagros Mountains at ~ 65 Ma to a possible break-off event of the Neo-Tethyan slab, some 25 Myr prior to any such within-plate type magmatism. 3) This break-off model was adopted by van der Meer *et al.* (2018) in ascribing an age of 65 ± 5 Ma to the 'top' of their Mesopotamia slab which can be seen in global mantle tomography model, with the 'top' age reflecting the time of detachment of the slab from the overlying lithosphere (Fig. 10). van der Meer *et al.* (2018) also designated this as the 'base' age of the Zagros slab seismic anomaly, where the Zagros slab was ascribed to renewed Tethyan subduction shortly after break-off of the Mesopotamia slab. We can now discuss a challenge to the timing or nature of these geodynamic scenarios, based on the scattered occurrence of Eocene within-plate type magmatism in the SaSiZ and wider geodynamic considerations. Firstly, the onset of voluminous magmatic activity in the UDMA and further east during the Eocene has already been ascribed to rollback-induced slab steepening (e.g. Verdel *et al.* 2007; 2011; Mouthereau *et al.* 2012). Verdel *et al.* (2011) argued that slab-rollback may have been preceded by a period of flat-slab subduction lasting from the mid-Cretaceous, as evidenced by a regional unconformity separating Cretaceous sediments from overlying Paleogene volcanic rocks (Stöcklin 1968). In this model, there need not have been a slab break-off event around the Cretaceous-Palaeogene boundary. Late Cretaceous deformation in the SaSiZ (Tillman *et al.* 1981) and a north-eastward shift in the locus of subduction-related magmatism from the SaSiZ to northern Iran and the UDMA also support the conclusion that a Tethyan slab was continuously attached to the surface during the mid-Cretaceous to Eocene (e.g., Guest *et al.* 2006; Omrani *et al.* 2008), albeit perhaps becoming shallower in angle at this time. Rapid exhumation in the Zagros mountains at ~65 Ma (Agard *et al.* 2011) could have several potential causes, including changes in collision rate or in the thickness and/or density of the subducted crust (Iannace *et al.* 2007; Brun & Faccenna 2008; Rosenbaum &

Mo 2011). Furthermore, an upsurge in mantle-derived magmatism is commonly ascribed in the literature to slab break-off. However, this upsurge is not recorded until 10's of Ma after the proposed break-off event of Agard *et al.* (2011), and as a corollary, nor did any extensive magmatism occur close to the Zagros Suture around ~65 Ma ago (Verdel *et al.* 2011).

Our understanding of the Eocene mafic rocks in the MBPC and the Piranshahr area provides a potential constraint on the issue described. The implication of the model of Verdel *et al.* (2011) is that during the Eocene, the Neo-Tethyan flat slab was rolling back towards the SW but did not roll back so far as to allow upwelling asthenosphere to flow beneath the SaSiZ. It seems difficult in this scenario for asthenosphere-derived magmas to be emplaced during the Late Eocene in the SaSiZ, given the proposed lack of a mantle wedge so close to the suture. Therefore, we feel that the most probable mechanism for igniting Late Eocene mafic magmatism in SaSiZ is a slab-tearing or detachment event concurrent with roll-back, perhaps related to subduction of a ridge or transform (Fig. 10). In such a scenario, a slab window would be generated whereby upwelling asthenosphere could rise past the slab, largely free of subduction-related fluids and/or melts, and thus partially melt at the base of the SaSiZ lithosphere. This slab-tearing, we propose, would lead to a Late Eocene break-off event rather than one at ~65 Ma. Widely-discussed models for slab window formation such as subduction of a spreading ridge orthogonal to the trench and/or lateral slab-tearing (Zandt & Humphreys 2008), seem unlikely processes. The first reason is that trench-orthogonal ridge subduction would lead to a narrow slab window which cannot explain the spread of SaSiZ magmatism, at sites some 500 km apart at similar times. Secondly, lateral slab-tearing is modelled to progress at hinge migration rates of ~25-155 km/Myr (Hale *et al.* 2010); implying there should be both a gap of ~3-20 Myr between magmatism in the MBPC and Pi, which does not exist as far as can be judged from the available geochronology. Trench-parallel subduction of a spreading ridge (see Zhang et al., in press) seems a more likely model. A brief lapse in 'normal' subduction processes during descent of the proposed spreading ridge might explain the limited occurrence of within-plate type rocks in the SaSiZ. Immediately after this short period of SaSiZ magmatism, subduction of the Zagros slab (after van der Meer *et al.* 2018) became established, and the locus of arc magmatism returned to the UDMA from the Latest Eocene to Oligocene (Verdel *et al.* 2011). This resumption of magmatism was short-lived, however, as it was followed by the Oligocene onset of continental collision between Arabia and the Central Iran Micro-Continent (e.g., McQuarrie & van Hinsbergen 2013) which resulted in a new magmatic shut-down.

In summary, we conclude that, whilst we support the flat-slab model of Verdel *et al.* (2011), we caution that the slab may not have been continuously subducting, but instead segmented and experienced break-off to form the Mesopotamia slab of van der Meer *et al.* (2018) during the Late Eocene. Subduction of Neo-Tethys then briefly resumed during the mid-Cenozoic and thus formed both the mid-Cenozoic UDMA and the young, shallow Zagros slab. Our new model requires revision of the 'top' age of the Mesopotamia slab and the 'base' age of the Zagros slab to ~45-40 Ma, and for the trigger of rapid exhumation of high pressure rocks in the Zagros around ~65 Myr ago (Agard *et al.* 2011) to be re-considered, perhaps as a consequence of a change in the nature of subducted crust at this time (e.g., Spikings & Simpson 2014).

Conclusions

Mafic magmatism in the N-SaSiZ includes suites of gabbroic dykes and plutons. In this study, we identified and studied two distinct generations of mafic-intermediate dykes in the MBPC. The first occurred in the Middle Jurassic and the second in the Late Eocene. These dykes and plutons preserved critical records of mantle source compositions and magma evolution from the MBPC, records which are not accessible from coeval felsic rocks.

Based upon geochemical and isotopic data, Middle Jurassic Group-1 dykes originated from metasomatized mantle peridotite containing garnet and spinel during active subduction of Neo-Tethys and evolved through fractional crystallization of clinopyroxene, plagioclase and apatite. They experienced degrees of mixing with crust-derived melt. The Late Eocene Group-2 dykes are products of low degree melting of asthenospheric mantle in the garnet-spinel transition zone. They appear to have undergone fractional crystallisation involving olivine, clinopyroxene, amphibole and apatite, but evidence for crustal assimilation is limited. Based upon U-Pb zircon ages, geochemical and isotopic data, it is concluded that during the Cretaceous and Paleocene, a period of flat-slab subduction took place, and the mantle wedge beneath the SaSiZ was removed from overriding plate. We concluded that the sub-parallel subduction of Neo-Tethys spreading ridge to the trench during Late Eocene, roll-back induced slab-tearing along the ridge axis, and subsequent break-off to generate the Mesopotamia slab, identified in the lower mantle by tomography studies. Break-off was followed by localised asthenospheric upwelling, which in turn fed within-plate magmatism in the N-SaSiZ, before short-lived re-establishment of Tethyan subduction and the resumption of arc magmatism in the UDMA, prior to the final Arabia-Eurasia collision. This final episode of subduction generated the Zagros slab which can be identified today in the mantle transition zone. Such a model is at odds with the continuous present of a subduction zone during the Cretaceous to Late Cenozoic or with a slab break-off event at ~65 Ma, but fits the magmatic record and could be adopted in current mantle tomography models (van der Meer *et al.* 2018).

Acknowledgements and funding

This research was financially supported by a grant from the Ministry of Science, Research and Technology of Iran and Payam Noor University. Zircon U-Pb dating was undertaken at Institute of Earth Sciences (IES), Academia Sinica, Taipei funded by Grant-in-Aid for Scientific Research #25400519 to RS. We gratefully acknowledge the critical comments by Charles Verdel and Bernard Bingen. We thank Majid Ghaderi, and Jean P. Liégeois for their comments on an early draft of the previous version of this manuscript. Sincere thanks also go to Stephen Daly, JGSL chief editor, for handling of the manuscript.

References

Agard, P., Omrani, J., Jolviet, L., Whitechurch, H., Vrielynck, B., Spakman, W., Monie, P., Meyer, B. & Wortel, R. 2011. Zagros orogeny: a subduction-dominated process. *Geological Magazine*, **148**, 5-6, 692–725, https://doi.org/10.1017/S001675681100046X.

Ahadnejad, V., Valizadeh, M.V., Deevsalar, R. & Rezaei-Kahkhaei, M. 2010. Age and geotectonic position of the Malayer granitoids: Implication for plutonism in the Sanandaj-Sirjan Zone, W Iran. *Neues Jahrbuch für Geologie und Paleontologie*, **261**, 61–75, https://doi.org/10.1127/0077-7749/2011/0149.

Ahmadi-Khalaji, A., Esmaeily, D., Valizadeh, M.V. & Rahimpour-Bonab, H. 2007. Petrology and geochemistry of the granitoid complex of Boroujerd, Sanandaj-Sirjan Zone, western Iran. *Journal of Asian Earth Sciences*, **29**, 859–877, https://doi.org/10.1016/j.seaes.2006.06.005.

Aldanmaz, E., Pearce, J.A., Thirlwall, M.F. & Mitchell, J.G. 2000. Petrogenetic evolution of Late Cenozoic, post-collision volcanism in western Anatolia, Turkey. *Journal of Volcanology and Geothermal Research*, **102**, 67–95, https://doi.org/10.1016/S0377-0273(00)00182-7.

Aldanmaz, E., Köprübas, N., Gürer, Ö.F., Kaymakc, N. & Gourgaud, A. 2006. Geochemical constraints on the Cenozoic, OIB-type alkaline volcanic rocks of NW Turkey: implications for mantle sources and melting processes. *Lithos*, **86**, 50–76, https://doi.org/10.1016/j.lithos.2005.04.003.

Allen, M. B., Kheirkhah, M., Neill, I., Emami, M. & McLeod, C. L. 2013. Generation of arc and within-plate chemical signatures in collision zone magmatism: Quaternary lavas from Kurdistan province, Iran. *Journal of Petrology*, **54**, 887–911, https://doi.org/10.1093/petrology/egs090.

Angiboust, S., Agard, P., Glodny, J., Omrani, J. & Oncken, O. 2016. Zagros blueschists: Episodic underplating and long-lived cooling of a subduction zone. *Earth and Planetary Science Letters*, **443**, 48-58. https://doi.org/10.1016/J.epsl.2016.03.017.

Azizi, H. & Moinevaziri, H. 2009. Review of the tectonic setting of Cretaceous to Quaternary volcanism in northwestern Iran. *Journal of Geodynamics*, **47**, 167–179, https://doi.org/10.1016/j.jog.2008.12.002.

Azizi, H., Zanjefili-Beiranvand, M. & Asahara, Y. 2015. Zircon U–Pb ages and petrogenesis of a tonalite–trondhjemite–granodiorite (TTG) complex in the northern Sanandaj–Sirjan zone, northwest Iran: Evidence for Late Jurassic arc–continent collision. *Lithos*, **216–217**, 178–195, https://doi.org/10.1016/j.lithos.2014.11.012.

Ballato, P., Nowaczyk, N.R., Landgraf, A., Strecker, M.R., Friedrich, A. & Tabatabaei, S.H. 2008. Tectonic control on sedimentary facies pattern and sediment accumulation rates in the Miocene foreland basin of the southern Alborz mountains, northern Iran. *Tectonics*, **27**, TC6001, https://doi.org/10.1029/2008TC002278.

Bartels, K. S., Kinzler, R.J. & Grove, T.L. 1991. High pressure phase relations of primitive high-alumina basalts from Medicine Lake volcano, northern California. *Contributions to Mineralogy and Petrology*, **108**, 253–270, https://doi.org/10.1007/BF00285935.

Brun, J-P. & Faccenna, C. 2008. Exhumation of high-pressure rocks driven by slab rollback. *Earth and Planetary Science Letters*. **272**, https://doi.org/10.1016/j.epsl.2008.02.03.

Chiu, H. Y., Chung, S. L., Zarrinkoub, M. H., Mohammadi, S., Khatib, M. M. & Iizuka Y. 2013. Zircon U–Pb age constraints from Iran on the magmatic evolution related to Neotethyan subduction and Zagros orogeny. *Lithos*, **162–163**, 70–87, https://doi.org/10.1016/j.lithos.2013.01.006.

Chang, J.M., Feeley, T.C. & Deraps, M.R. 2009. Petrogenesis of basaltic volcanic rocks from the Pribilof Islands, Alaska, by melting of metasomatically enriched depleted lithosphere, crystallization differentiation, and magma mixing. *Journal of Petrology*, **50**, 2249–228, https://doi.org/10.1093/petrology/egp075.

Davies, J.H. & von Blanckenburg, F. 1995. Slab breakoff: A model of lithosphere detachment and its test in the magmatism and deformation of collisional orogens. *Earth and Planetary Science Letters*, **129**, 85-102, https://doi.org/10.1016/0012-821X(94)00237-1.

DePaolo, D. J. & Daley, E. E. 2000. Neodymium isotopes in basalts of the Southwest Basin and Range and lithospheric thinning during continental extension. *Chemical Geology*, **169**, 157–185, https://doi.org/10.1016/S0009-2541(00)00261-8.

Deevsalar, R., Ghorbani, M.R., Ghaderi, M., Ahmadian, J., Murata, M., Ozawa, H. & Shinjo, R. 2014. Geochemistry and petrogenesis of arc-related to intraplate mafic magmatism from the Malayer-Boroujerd plutonic complex, northern Sanandaj-Sirjan Zone, Iran. *Neues Jahrbuch für Geologie und Paleontologie*, **274**, 81–120, https://doi.org/10.1127/njgpa/2014/0435.

Deevsalar, R., Shinjo, R., Ghaderi, M, Murata., M., Hoskin, P.W.O., Oshiro, S., Wang, K.L., Lee, H.Y. & Neill, I. 2017. Mesozoic-Cenozoic mafic magmatism in Sanandaj-Sirjan Zone, Zagros Orogen (Western Iran): geochemical and isotopic inferences from Middle Jurassic and Late Eocene gabbros. *Lithos*, **284–285**, 588–607, https://doi.org/10.1016/j.lithos.2017.05.009.

Deevsalar, R., Shinjo, R., Liégeois, J. P., Valizadeh, J. P., Ahmadian, J., Yeganehfar, H., Murata, M., Neill, I. (2018). Subduction-related mafic to felsic magmatism in the Malayer-Boroujerd plutonic complex, western Iran. *Swiss Journal of Geosciences*, **111**, 269-293, https://doi.org/10.1007/s00015-017-0287-y.

Dilek, Y. & Sandvol, E., 2009. Seismic structure, crustal architecture and tectonic evolution of the Anatolian–African Plate Boundary and the Cenozoic Orogenic Belts in the Eastern Mediterranean Region. *In*: Murphy, J.B., Keppie, J.D., Hynes, A.J. (eds) *Ancient Orogens and Modern Analogues*. Geological Society, London: Special Publications, **327**, 127–160, https://doi.org/10.1144/SP327.8.

Draper, D. S. & Johnston, A. D. 1992. Anhydrous PT phase relations of an Aleutian high-MgO basalt: an investigation of the role of olivine-liquid reaction in the generation of arc high-alumina basalts. *Contributions to Mineralogy and Petrology*, **112**, 501–519, https://doi.org/10.1007/BF00310781.

Ekici, T., Macpherson, C.G., Otlu, N. & Fontignie, D. 2014. Foreland magmatism during the Arabia–Eurasia collision: Pliocene–Quaternary activity of the Karacadag Volcanic Complex, SW Turkey. *Journal of Petrology*, **55**, 1753–1777, https://doi.org/10.1093/petrology/egu040.

Ellam, R.M. & Hawkesworth, C.J. 1988. Elemental and isotopic variations in subduction related basalts: Evidence for a three component model. *Contributions to Mineralogy and Petrology*, **98**, 72–80, https://doi.org/10.1007/BF00371911.

Floyd, P.A. & Winchester, J.A. 1975. Magma type and tectonic setting discrimination using immobile elements. *Earth and Planetary Science Letters*, **27**, 211–218, https://doi.org/10.1016/0012-821X(75)90031-X.

Ghaffari, M., Rashidnejad-Omran, N., Dabiri, R., Chen, B. & Santos, J. F. 2013. Mafic–intermediate plutonic rocks of the Salmas area, northwestern Iran: their source and petrogenesis significance. *International Geology Review,* **55**, 2016–2029, https://doi.org/10.1080/00206814.2013.817067.

Ghalamghash, J., Vousoughi Abedini, M., Bellon, H., Emami, M.H., Pourmafi, M. & Rashid, H. 2003. K/Ar age dating of Oshnavieh plutonic complex. *Geosciences*, **11** (47-48), 16–27.

Ghalamghash, J., Nédélec, A., Bellon, H., Vousoughi-Abedini, M. & Bouchez, J.L. 2009a. The Urumieh plutonic complex (NW Iran): a magmatic record of the geodynamic evolution of the Sanandaj–Sirjan zone during Cretaceous times – Part I: Petrogenesis and K/Ar dating. *Journal of Asian Earth Sciences*, **5**, 401–415, https://doi.org/j.jseaes.2009.02.002.

Gorring, M. L., Kay, S. M., Zeitler, P. K., Ramos, V. A., Rubiolo, D., Fernández, M. I. & Panza, J. L. 1997. Neogene Patagonian plateau lavas: continental magmas associated with ridge collision at the Chile Triple Junction. *Tectonics*, **16**, 1-17, https://doi.org/10.1029/96TC03368.

Guest, B., Stockli, D. F., Grove, M., Axen, G.J., Lam, P.S. & Hassanzadeh, J. 2006. Thermal histories from the central Alborz Mountains, northern Iran: implications for the spatial and temporal distribution of deformation in northern Iran. *Geological Society of America Bulletin*, **118**, 1507-1521, https://doi.org/10.1130/B25819.1.

Hale, A.J., Gottschaldt, K.-D., Rosenbaum, G., Bourgouin, L., Bauchy, M. & Mühlhaus, H. 2010. Dynamics of slab tear faults: Insights from numerical modelling. *Tectonophysics*, **483**, 58-70, https://doi.org/10.1016/j.tecto.2009.05.019.

Hanson, G. N. 1978. The application of trace elements to the petrogenesis of igneous rocks of granitic composition. *Earth and Planetary Science Letters*, **38**, 26–43, https://doi.org/10.1016/0012-821X(78)90124-3.

Hastie, A. R., Kerr, A.C., Pearce, J.A. & Mitchell, S.F. 2007. Classification of altered island arc rocks using immobile trace elements: development of the Th-Co discrimination diagram. *Journal of Petrology*, **48**, 2341-2357, https://doi.org/10.1093/petrology/egm062.

Hastie, A.R., Mitchell, S.F., Kerr, A.C., Minifie, M.J. & Millar, I.L. 2011. Geochemistry of rare high-Nb basalt lavas: are they derived from a mantle wedge metasomatised by slab melts? *Geochimica et Cosmochimica Acta*, **75**, 5049–5072, https://doi.org/10.1016/j.gca.2011.06.018.

Hastie, A. R., Mitchell, S. F., Treloar, P., Kerr, A. C., Neill, I. & Barfod, D. N. 2013. Geochemical components in a Cretaceous island arc: The Th/La:$(Ce/Ce^*)_{Nd}$ diagram and implications for subduction initiation in the inter-American region. *Lithos*, **162**, 57-69, https://doi.org/10.016/j.lithos.2012.12.001.

Hofmann, A.W. 2005. Sampling mantle heterogeneity through oceanic basalts: isotopes and trace Elements. *In:* Carlson, R.W. (ed) *The mantle and core*. Treatise on Geochemistry, Elsevier, Amsterdam, **2**, 61–101, https://doi.org/10.1016/B0-08-043751-6/02123-X.

Hoskin, P.W.O. & Schaltegger, U. 2003. The compositions of zircon and igneous and metamorphic petrogenesis. *Reviews in Mineralogy and Geochemistry*, **53**, 27–55, https://doi.org/10.2113/0530027.

Iannace, A., Vitale, S., D'errico, M., Mazzoli, S., Di Staso, A., Macaione, E., Messina, A., Reddy, S.M., Somma, R., Zamparelli, V., Zattin, M., & Bonardi, G. 2007. The carbonate tectonic units of northern Calabria (Italy): a record of Apulian and palaeomargin evolution and Miocene convergence, continental crust subduction, exhumation of HPLT rocks. *Journal of the Geological Society*, **164**; 1165-1186, https://doi.org/10.1144/0016-76492007-017.

Ionov, D.A. & Hofmann, A.W. 1995. Nb-Ta-rich mantle amphiboles and micas: Implications for subduction-related metasomatic trace element fractionations. *Earth and Planetary Science Letters*, **131**, 341–356, https://doi.org/10.1016/0012-821X(95)00037-D.

Ireland, T.R. & Williams, I.S. 2003. Considerations in zircon geochronology by SIMS. *In:* Manchar, J.M., Hoskin, P.W.O. (eds) *Zircon*. *Reviews of Mineralogy and Geochemistry*, **53**, 215–241, https://doi.org/10.2113/0530215.

Jaques, A.L. & Green, D.H. 1980. Anhydrous melting of peridotite at 0-15 kbar pressure and the genesis of tholeiitic basalts. *Contributions to Mineralogy and Petrology*, **73**, 287-310, https://doi.org/10.1007/BF00381447.

Jahn, B.-M., Wu, F.-Y. & Lo, C.-H. 1999. Crust–mantle interaction induced by deep subduction of the continental crust: geochemical and Sr–Nd isotopic evidence from post-collisional mafic-ultramafic intrusions of the northern Dabie Complex, Central China. *Chemical Geology*, **157**, 119–146, https://doi.org/10.1016/S0009-2541(98)00197-1.

Jiang Y.-H., Jiang, S.-Y., Ling, H.-F. & Ni, P. 2010. Petrogenesis and tectonic implications of Late Jurassic shoshonitic lamprophyre dikes from the Liaodong Peninsula, NE China. *Mineralogy and Petrology*, **100**, 127–151, https://doi.org/10.1007/s00710-010-0124-8.

John, T., Scherer, E.E., Haase, K. & Schenk, V. 2004. Trace element fractionation during fluid-induced eclogitization in a subducting slab: trace element and Lu–Hf–Sm–Nd isotope systematics. *Earth and Planetary Science Letters*, **227**, 441–456, https://doi.org/10.1016/j.epsl.2004.04.009.

Kelemen, P.B., Yogodzinski, G.M. & Scholl, D.W. 2003. Along-strike variation in the Aleutian Island Arc: genesis of high Mg# andesite and implications for continental crust. *In:* Eiler, J. (ed) *Inside the Subduction Factory*. AGU, Washington, 223–276, https://doi.org/10.1029/138GM11.

Kheirkhah, M., Neill, I., Allen, M.B. & Ajdari, K. 2013. Small-volume melts of lithospheric mantle during continental collision: Late Cenozoic lavas of Mahabad, NW Iran. *Journal of Asian Earth Sciences*, **74**, 37–49, https://doi.org/10.1016/j.jseaes.2013.06.002.

Kheirkhah, M., Neill, I. & Allen, M.B. 2015. Petrogenesis of OIB-like basaltic volcanic rocks in a continental collision zone: Late Cenozoic magmatism of Eastern Iran. *Journal of Asian Earth Sciences*, **106**, 19-33, https://doi.org/10.1016/j.jseaes.2015.02.027.

Langmuir, C.H., Vocke Jr, R.D., Hanson, G.N. & Hart, S.R. 1978. A general mixing equation with applications to Icelandic basalts. *Earth and Planetary Science Letters*, **37**, 380–392, https://doi.org/10.1016/0012-821X(78)90053-5.

Lassiter, J.C., Hauri, E.H., Reiners, P.W. & Garcia, M.O. 2000. Generation of Hawaiian post-erosional lavas by melting of a mixed lherzolite/pyroxenite source. *Earth and Planetary Science Letters*, **178**, 269–284, https://doi.org/10.1016/S0012-821X(00)00084-4.

Lundstrom, C.C., Hoernle, K. & Gill, J. 2003. U-series disequilibria in volcanic rocks from the Canary Islands: plume versus lithospheric melting. *Geochimica et Cosmochimica Acta*, **67**, 4153–4177, https://doi.org/10.1015/S0016-7037(03)00308-9.

Macdonald, R., Rogers, N.W., Fitton, J.G., Black, S. & Smith, M. 2001. Plume-lithosphere interactions in the generation of the basalts of the Kenya rift, east Africa. *Journal of Petrology*, **42**, 877–900, https://doi.org/10.1093/petrology/42.5.877.

Macpherson, C.G., Dreher, S.T. & Thirlwall, M.F. 2006. Adakites without slab melting: high pressure processing of basaltic island arc magma, Mindanao, the Philippines. *Earth and Planetary Science Letters*, **243**, 581–593, https://doi.org/10.1016/j.epsl.2005.12.034.

McQuarrie, N. & van Hinsbergen, D.J.J. 2013. Retrodeforming the Arabia-Eurasia collision zone: Age of collision versus magnitude of continental subduction. *Geology*, **41**, 315-318, https://doi.org/10.1130/G33591.1.

Mederer, J., Moritz, R., Ulianov, A. & Chiaradia, M. 2013. Middle Jurassic to Cenozoic evolution of arc magmatism during Neotethys subduction and arc-continent collision in the Kapan Zone, southern Armenia. *Lithos*, **177**, 61–78, https://doi.org/10.1016/j.lithos.2013.06.005.

Mahmoudi, S., Corfu, F., Masoudi, F., Mehrabi, B. & Mohajjel, M. 2011. U–Pb dating and emplacement history of granitoid plutons in the northern Sanandaj–Sirjan Zone, Iran. *Journal of Asian Earth Sciences*, **41**, 238–249, https://doi.org/10.1016/j.jseaes.2011.03.006.

Masoudi, F. 1997. Contact metamorphism and pegmatite development in the region SW of Arak, Iran, Unpublished PhD thesis, University of Leeds, UK, 231 pp.

Mazhari, S.A., Bea, F., Amini, S., Ghalamghash, J., Molina, J.F., Montero, P., Scarrow, J.H. & Williams, I.S. 2009. The Eocene bimodal Piranshahr massif of the Sanandaj–Sirjan Zone, NW Iran: a marker of the end of the collision in the Zagros orogeny. *Journal of the Geological Society of London*, **166**, 53–69, https://doi.org/10.1144/0016-76492008-022.

Mazhari, S.A, Amini, S., Ghalamghash, J. & Bea, F. 2011. Petrogenesis of granitic unit of Naqadeh complex, Sanandaj– Sirjan Zone, NW Iran. *Arabian Journal of Geosciences*, **4**, 59–67, https://doi.org/10.1007/s12517-009-0077-6.

McDonough, W.F. & Sun, S.-S. 1995. Composition of the Earth. *Chemical Geology*, **120**, 223–253, https://doi.org/10.1016/0009-2541(94)00140-4.

McKenzie, D. & O'Nions, R. K. 1991. Partial melt distributions from inversion of rare earth element concentrations. *Journal of Petrology*, **32**, 1021–1091, https://doi.org/10.1093/petrology/32.5.1021.

Miller, K.G., Kominz, M.A., Browning, J.V., Wright, J.D., Mountain, G.S., Katz, M.E., Sugarman, J., Cramer, B.S., Christie-Blick N. & Pekar, S.F. 2005. The Phanerozoic record of global sea-level change. *Science*, **310**, 1293–1298, https://doi.org/10.1126/science.1116412.

Mohajjel, M. & Fergusson, C. L. 2014. Jurassic to Cenozoic tectonics of the Zagros Orogen in northwestern Iran. *International Geology Review*, **56**, 263–287, https://doi.org/10.1080/00206814.2013.853919.

Mouthereau, F., Lacombe, O. & Vergés, J. 2012. Building the Zagros collisional orogeny: Timing, strain distribution and the dynamics of Arabia/Eurasia convergence. *Tectonophysics*, **532**, 27–60, https://doi.org/10.1016/j.tecto.2012.01.022.

Nakamura, N. 1974. Determination of REE, Ba, Fe, Mg, Na and K in carbonaceous and ordinary chondrites. *Geochimica et Cosmochimica Acta*, **38**, 757–775, https://doi.org/10.1016/0016-7037(74)90149-5.

Neill, I., Meliksetian, Kh., Allen, M.B., Navasardyan, G. & Karapetyan, S. 2013. Pliocene–Quaternary volcanic rocks of NW Armenia: magmatism and lithospheric dynamics within an active orogenic plateau. *Lithos*, **180–181**, 200–215, https://doi.org/10.1016/j.lithos.2013.05.005.

Neill, I., Meliksetian, K., Allen, M. B., Navasardyan, G. & Kuiper, K. 2015. Petrogenesis of mafic collision zone magmatism: The Armenian sector of the Turkish–Iranian Plateau. *Chemical Geology*, **403**, 24–41, https://doi.org/10.1016/j.chemgeo.2015.03.013.

Nesbitt, H.W. & Young, G.M. 1982. Early Proterozoic climates and plate motions inferred from major element chemistry of lutite. *Nature*, **299**, 715–717, https://doi.org/10.1038/299715a0.

Omrani, J., Agard, P., Whitechurch, H., Benoit, M., Prouteau, G. & Jolivet, L. 2008. Arc magmatism and subduction history beneath the Zagros Mountains, Iran: a new report of adakites and geodynamic consequences. *Lithos*, **106**, 380–398, https://doi.org/10.1016/j.lithos.2008.09.008.

Pearce, J. A. 1983. Role of the sub-continental lithosphere in magma genesis at active continental margins. *In:* Hawkesworth, C. J. & Norry, M. J. (eds) *Continental Basalts and Mantle Xenoliths*. Shiva Publishing Ltd., Cambridge, Mass., 230-249.

Pearce, J.A. & Peate, D.W. 1995. Tectonic implications of the composition of volcanic arc magmas. *Annual Review of Earth and Planetary Sciences*, **23**, 251-285, https://doi.org/10.1146/annurev.ea.23.050195.001343.

Plank, T., & Langmuir, C.H. 1998. The chemical composition of subducting sediment: Implications for the crust and mantle. *Chemical Geology*, **145**, 325–394, https://doi.org/10.1016/S0009-2541(97)00150-2.

Ramos, V.A. & Kay, S.M. l992. Southern Patagonian plateau basalts and deformation: backarc testimony of ridge collision. *Tectonophysics*, **205**, 261–282, https://doi.org/10.1016/0040-1951(92)90430-E.

Ramkumar, Mu. 2015. Chemostratigraphy: Concepts, Techniques, and Applications. Amsterdam: Elsevier.

Rashidnejad-Omran, N., Emami, M.H., Sabzehi, M., Rastad, E., Belon, H. & Pique, A. 2002. Lithostratigraphie et histoire paléozoïque à Paléocène des complexes métamorphiques de la région de Muteh, zone de Sanandaj–Sirjan (Iran meridional). *Comptes Rendus Geoscience*, **334**, 1185–1191, https://doi.org/10.1016/S1631-0713(02)01861-8.

Rosenbaum, G. & Mo, W. 2011. Tectonic and magmatic responses to the subduction of high bathymetric relief. *Gondwana Research*, **19**, 571–582, https://doi.org/10.1016/j.gr.2010.10.007.

Sepahi, A.A. 2008. Typology and petrogenesis of granitic rocks in the Sanandaj-Sirjan metamorphic belt, Iran: with emphasis on the Alvand plutonic complex. *Neues Jahrbuch für Geologie und Paleontologie*, **247**, 295–312, https://doi.org/10.1127/0077-7749/2008-0247-0295.

Sepahi, A.A., Shahbazi, H., Siebel, W. & Ranin, A. 2014. Geochronology of plutonic rocks from the Sanandaj-Sirjan Zone, Iran and new zircon and titanite U-Th-Pb ages for granitoids from the Marivan pluton. *Geochronometria*, **41**, 207–215, https://doi.org/10.2478/s13386-013-0156-z.

Sepahi, A.A., Salami, S., Lentz, D., McFarlane, C. & Maanijou, M. (in press). Petrography, geochemistry, and U–Pb geochronology of pegmatites and aplites associated with the Alvand intrusive complex in the Hamedan region, Sanandaj–Sirjan zone, Zagros orogen (Iran). *International Journal of Earth Sciences*, https://doi.org/10.1007/s00531-017-1515-4.

Shahbazi, H., Siebel, W., Pourmoafee, M., Ghorbani, M., Sepahi, A.A., Shang, C.-K. & Vousoughi Abedini, M. 2010. Geochemistry and U–Pb zircon geochronology of the Alvand plutonic complex in Sanandaj–Sirjan Zone Iran: New evidence for Jurassic magmatism. *Journal of Asian Earth Sciences*, **39**, 668–683, https://doi.org/10.1016/j.seaes.2010.04.014.

Shaw, D.M. 1970. Trace element fractionation during anatexis. *Geochimica et Cosmochimica Acta*, **34**, 237–243, https://doi.org/10.1016/0016-7037(70)90009-8.

Shimuda, G. 2009. Genetic link between EMI and EMII: An adakite connection. *Lithos*, **112**, 591–602, https://doi.org/10.1016/j.lithos.2009.05.025.

Spikings, R. & Simpson, G. 2014. Rock uplift and exhumation of continental margins by the collision, accretion, and subduction of buoyant and topographically prominent ocean crust. *Tectonics*, **33**, 635-655, https://doi.org/10.1002/2013TC003425.

Stampfli, G. M. & Borel, G. D. 2002. A plate tectonic model for the Paleozoic and Mesozoic constrained by dynamic plate boundaries and restored synthetic oceanic isochrons. *Earth and Planetary Science Letters*, **196**, 17–33, https://doi.org/10.1016/S0012-821X(01)00588-X.

Stöcklin, J. 1968. Structural history and tectonics of Iran: a review. *AAPG Bulletin*, **52**, 1229–1258, https://doi.org/10.1306/5D25C4A5-16C1-11D7-8645000102C1865D.

Streckeisen, A.L. & Le Maitre, R.W. 1979. A chemical approximation to the modal QAPF classification of the igneous rocks. *Neues Jahrbuch fur Mineralogie*, **136**, 169–206.

Sun, S.-S. & McDonough, W.F. 1989. Chemical and isotopic systematics of oceanic basalts: implications for mantle composition and processes. *In:* Saunders, A.D. & Norry, M.J. (eds) *Magmatism in the Ocean Basins*. Geological Society of London, Special Publications, **42**, 313–345, https://doi.org/10.1144/GSL.SP.1989.042.01.19.

Taylor, S.R. & McLennan, S.M. 1985. The continental crust: its composition and evolution. Blackwell Scientific Publications, Oxford, 328 pp.

Tera, F. & Wasserburg, G.J. 1972. U–Th–Pb systematics in three Apollo 14 basalts and the problem of initial Pb in lunar rocks. *Earth and Planetary Science Letters*, **14**, 281–304, 10.1016/0012-821X(72)90128-8.

Turner, S., Hawkesworth, C., Rogers, N., Bartlett, J., Worthington, T., Hergt, J., Pearce, J. & Smith, I. 1997. ^{238}U–^{230}Th disequilibrium, magma petrogenesis, and flux rates beneath the depleted Tonga-Kermadec island arc. Geochimica et Cosmochimica Acta, **61**, 4855–4884, https://doi.org/10.1016/S0016-7037(97)00281-0.

van der Meer, D.G., van Hinsbergen, D.J.J. & Spakman, W. 2018. Atlas of the underworld: slab remnants in the mantle, their sinking history, and a new outlook on lower mantle viscosity. *Tectonophysics*, **723**, 309-448, https://doi.org/10.1016/j.tecto.2017.10.004.

Verdel, C., Wernicke, B.P., Hassanzadeh, J. & Guest, B. 2011. A Paleogene extensional arc flare-up in Iran: *Tectonics*, **30**, TC3008, https://doi.org/10.1029/2010TC002809.

Verdel, C., Wernicke, B.P., Ramezani, J., Hassanzadeh, J., Renne, P.R. & Spell, T.L. 2007. Geology and thermochronology of Tertiary Cordilleran-style metamorphic core complexes in the Saghand region of central Iran. *Geological Society of America Bulletin*, **119**, 961–977, https://doi.org/10.1130/B26101.1.

Wedepohl, K.H. 1995. The composition of the continental crust. *Geochimica et Cosmochimica Acta*, **59**, 1217-1232, https://doi.org/10.1016/0016-7037(95)00038-2.

Winchester, J. A. & Floyd, P.A. 1977. Geochemical discrimination of different magma series and their differentiation products using immobile elements. *Chemical Geology*, **20**, 325-344, https://doi.org/10.1016/0009-2541(77)90057-2.

Wittke, J. H. & Mack, L. E. 1993. OIB-like mantle source for continental alkaline rocks of the Balcones province, Texas: trace-element and isotopic evidence. *Journal of Petrology*, **101**, 333–344, https://doi.org/10.1086/648227.

Zandt, G. & Humphreys, E. 2008. Toroidal mantle flow through the western U.S. slab window. *Geology*, **36**, 295-298, https://doi.org/10.1130/G24611A.1.

Zhang, H.F., Sun, M., Zhou, X.H., Fan, W.M., Zai, M.G. & Ying, J.F. 2002. Mesozoic lithosphere destruction beneath the North China Craton: evidence from major-, trace -element and Sr–Nd–Pb isotope studies of Fangcheng basalts. *Contributions to Mineralogy and Petrology*, **144**, 241–253, https://doi.org/10.1007/s00410-002-0395-0.

Zhang, Z., Xiao, W., Ji, W., Majidifard, M.R., Rezaeian, M., Talebian, M., Xiang, D., Chen, L., Wan, B., Ao, S. & Esmaeili, R. in press. Geochemistry, zircon U-Pb and Hf isotope for granitoids, NW Sanandaj-Sirjan zone, Iran: Implications for Mesozoic-Cenozoic episodic magmatism during Neo-Tethyan lithospheric subduction. Gondwana Research, http://doi.org/10.1016/j.gr.2018.04.002.

Table 1
Whole rock chemical composition of the MBPC dykes (major oxides in wt. %, trace elements in ppm).

	Group-1: Middle Jurassic dykes						Group-2: Late Eocene dykes					
	Gabbro			Diorite			Gabbro					
Location	**MN2a**	**MN8**	**BR03b*[1]**	**BR02*[1]**	**BR07**	**M23*[1]**	**M33*[1]**	**MN04**	**M29*[1]**	**MN12**	**MN13**	**MN07**
X	48.76006	48.80782	48.81201	48.80916	48.93265	48.85036	48.81733	48.80776	48.75991	48.76612	48.77025	48.80722
Y	34.14333	34.10255	33.97396	33.97642	33.74269	34.06678	34.10433	34.12035	34.14344	34.08282	34.08297	34.11624
	wt.%											
SiO_2	51.84	45.45	46.93	59.56	52.25	59.39	49.34	48.40	47.04	46.91	47.53	47.33
TiO_2	0.49	3.70	1.90	0.97	1.62	0.96	1.91	2.21	2.44	2.27	2.58	2.58
Al_2O_3	12.61	15.16	16.39	19.6	17.19	19.78	17.36	17.67	14.88	16.01	16.45	16.16
FeO^T	7.25	12.26	11.15	8.07	9.07	7.41	9.98	10.55	12.05	10.76	11.56	12.08
MnO	0.18	0.21	0.18	0.09	0.15	0.09	0.17	0.21	0.20	0.20	0.19	0.20
MgO	9.75	5.01	6.89	2.31	4.00	2.36	5.08	5.15	4.90	5.10	5.02	5.62
CaO	11.51	8.93	9.79	0.35	7.21	0.34	9.70	9.56	9.55	9.25	10.27	9.39
Na_2O	1.51	3.22	2.98	0.69	2.29	0.68	3.52	3.22	3.02	2.87	3.34	3.14
K_2O	1.15	1.05	0.92	4.65	1.90	4.74	1.38	1.33	0.80	1.35	1.05	1.38
P_2O_5	0.04	0.69	0.31	0.14	0.34	0.14	0.46	0.52	0.55	0.60	0.71	0.77
LOI	2.86	3.02	2.13	3.62	2.60	4.03	0.68	0.85	3.52	3.67	1.10	1.26
Total	99.19	98.7	99.57	100.05	98.62	99.92	99.58	99.67	98.95	98.99	99.8	99.91
$Mg^{\#}$	0.57	0.29	0.38	0.22	0.29	0.24	0.34	0.33	0.29	0.32	0.30	0.32
	ppm											
Cs	2.62	12.04	8.12	14.08	20	14.30	2.80	1.77	2.20	1.50	1.28	1.84
Rb	34.70	147	151.40	216.1	141.60	205.7	40.1	44.04	17.64	50.26	31.27	29.79
Ba	136	219.40	427.60	478	341	533.0	332	273.00	142	265.40	187.50	79.70
Th	6.75	14.07	16.55	16.67	15.68	17.10	4.50	1.42	1.67	2.12	1.41	1.43
U	1.41	1.93	1.60	1.76	2.02	2.70	0.90	0.30	0.36	0.48	0.34	0.31
Nb	7.07	14.36	17.47	17.91	15.56	16.10	29.30	16.55	19.64	16.99	19.62	17.17
Pb	14.36	22.42	28.35	8.87	22.04	2.95	1.87	7.75	10.83	3.76	3.63	5.74
Sr	82.7	83.52	102.6	93.31	89.22	48.10	625.00	415.1	482.5	438.3	453.1	445.9
Hf	3.78	5.10	5.03	4.97	4.90	4.90	1.00	1.11	1.05	1.36	1.16	0.77
Zr	84	263.2	149.50	200.5	161.8	196.9	189.50	144.8	151.6	160	147	152
Ta	0.60	1.29	1.41	1.49	1.51	1.20	1.70	1.34	1.45	1.20	1.48	1.37
Y	31.66	11.16	9.81	9.59	20.46	31.10	24.70	26.07	28.89	29.60	29.03	26.69
Cr	904.00	131.10	140.10	153.40	119.40	83.70	85.61	79.07	85.61	101.50	54.96	79.62
Ni	273.10	44.81	48.21	59.45	47.62	57.10	32.91	32.09	32.91	39.25	26.53	29.83
Co	37.06	17.11	17.42	19.81	18.95	17.60	38.61	35.59	38.61	37.69	32.49	34.42
V	198.80	142.20	149.80	179.20	143.90	115	241.50	227.20	241.50	217.70	180.90	230.50
La	19.79	38.84	45.12	46.3	41.82	46.3	33.90	18.39	20.04	20.67	25.04	15.71
Ce	44.39	81.92	93.03	93.2	87.2	91	61.70	39.19	42.45	44.13	51.13	34.07
Pr	6.058	9.03	10.20	10.12	9.769	10.11	6.77	5.032	5.441	5.702	6.334	4.373
Nd	25.38	23.4	37.43	19.9	19.1	18.6	25.20	21.79	23.87	25.09	27.31	19.06
Sm	5.977	5.19	6.69	4.78	4.76	4.35	5.24	5.188	5.634	5.938	6.225	4.797
Eu	1.274	2.21	1.37	1.65	1.67	1.53	1.81	1.749	2.104	2.343	2.268	1.532
Gd	5.328	5.48	5.09	5.35	5.3	4.76	5.71	5.187	5.427	5.868	5.953	4.919
Tb	0.9065	0.8	0.62	0.79	0.8	0.72	0.83	0.8493	0.9036	0.947	0.9833	0.8358
Dy	5.624	4.44	2.68	4.43	4.69	5.06	4.57	5.087	5.332	5.573	5.627	5.054
Ho	1.123	0.85	0.40	0.88	1	0.89	0.98	0.9626	1.045	1.056	1.087	0.9727
Er	3.207	2.48	0.84	2.79	2.63	2.4	2.41	2.532	2.808	2.765	2.811	2.612
Tm	0.4683	0.33	0.10	0.34	0.36	0.34	0.38	0.3406	0.375	0.3679	0.3694	0.3537
Yb	2.957	2.01	0.53	2.22	2.09	2.21	2.37	1.971	2.228	2.157	2.12	2.067
Lu	0.4164	0.29	0.07	0.31	0.34	0.29	0.34	0.2563	0.3032	0.2844	0.2693	0.2803
∑REE	122.90	177.27	204.17	193.06	181.53	188.56	152.21	108.52	117.96	122.89	137.53	96.64
Nb/Y	0.22	1.29	1.78	1.87	0.76	0.52	1.19	0.63	0.68	0.57	0.68	0.64
Zr/Nb	11.88	18.33	8.56	11.19	10.40	12.23	6.47	8.75	7.72	9.42	7.49	8.85
K/Nb	1350.7	607.04	437.19	2235.2	1013.7	2548.5	389.9	667.16	338.16	659.66	444.29	667.25
Ba/Nb	19.24	15.28	24.48	26.69	21.92	33.11	11.33	16.50	7.23	15.62	9.56	4.64
La/Nb	2.80	2.70	2.58	2.59	2.69	2.88	1.16	1.11	1.02	1.22	1.28	0.91
Ce/Ce*	1.00	1.07	0.85	1.03	1.05	1.01	0.98	0.98	0.97	0.96	0.97	0.99

LOI: loss on ignition
FeO*: Total Fe is represented as FeO.
Ce/Ce* is calculated by $Ce_{CN}/La_{CN}{}^{2/3} \times Nd_{CN}{}^{1/3}$.
*[1] Major elements determined by XRF in Naruto University, Japan; and trace elements by ICP-MS in ACME laboratory, Canada. Other data were produced in University of the Ryukyus.

	Group-2: Late Eocene dykes									
	Gabbro									
Location	M34*2	M37*2	M50*2	M25b*2	M54*2	M38*2	M58*2	M22*2	BR04*2	BR03d*2
X	48.81394	48.81497	48.67419	48.86703	48.57739	48.82069	48.69875	48.87164	48.24472	48.81139
Y	34.10503	34.10214	34.22044	34.08203	34.28564	34.09997	34.23411	34.07728	33.56667	33.97397
	wt.%									
SiO_2	47.99	48.67	46.97	48.03	46.68	47.97	48.77	46.98	48.06	48.11
TiO_2	2.10	1.89	2.63	2.03	3.80	1.96	2.08	3.20	1.87	1.88
Al_2O_3	16.78	16.97	15.61	16.75	14.33	16.31	17.12	15.46	17.02	16.88
FeO^T	10.67	10.76	11.65	10.36	13.90	10.96	9.80	12.17	10.19	10.20
MnO	0.17	0.15	0.21	0.16	0.22	0.17	0.15	0.19	0.17	0.18
MgO	5.96	6.65	5.21	6.13	4.06	7.17	5.08	6.30	7.09	7.16
CaO	10.70	9.50	11.18	10.78	9.48	10.21	10.41	9.93	10.04	10.07
Na_2O	3.16	2.81	1.67	3.25	3.98	3.00	3.82	2.96	3.20	3.13
K_2O	0.91	1.08	3.00	0.98	0.86	0.69	1.17	0.96	0.94	0.94
P_2O_5	0.38	0.34	0.56	0.36	1.16	0.33	0.52	0.48	0.27	0.31
LOI	0.91	0.68	0.66	0.87	1.1	1.01	0.93	1.05	0.96	0.87
Total	99.73	99.5	99.35	99.7	99.57	99.78	99.85	99.68	99.81	99.73
$Mg^\#$	0.36	0.38	0.31	0.37	0.23	0.40	0.34	0.34	0.41	0.41
	ppm									
Cs	1.90	5.00	1.70	1.90	1.30	1.30	2.20	3.00	1.60	1.80
Rb	10.90	30.00	118.00	17.90	30.10	13.70	20.30	22.50	34.10	34.30
Ba	152	183	312	175	170	107	298	228	107	116
Th	1.70	2.60	1.90	1.60	2.50	1.30	1.50	2.50	1.30	1.60
U	0.50	0.70	0.60	0.40	1.10	0.30	0.50	0.70	0.30	0.40
Nb	18.10	16.60	20.50	15.20	27.30	14.20	15.20	21.70	11.50	11.90
Pb	2.92	3.30	11.29	2.43	5.30	2.76	2.81	1.38	1.49	1.88
Sr	467.70	474.40	427.20	524.80	368.50	464.00	619.60	450.40	424.10	444.00
Hf	1.49	1.60	1.51	1.72	1.23	1.42	0.71	1.26	0.81	1.31
Zr	141.60	152.40	144.60	139.70	197.60	130.50	124.60	201.60	156.70	159.10
Ta	1.30	1.20	1.30	1.00	2.00	0.90	1.00	1.30	0.90	0.80
Y	24.00	26.30	24.80	27.10	37.20	22.00	23.50	34.80	27.00	27.40
Cr	9.30	38.40	43.10	13.50	1.70	3.50	10.20	9.70	23.70	111.10
Ni	17.80	38.60	25.90	19.60	5.40	26.40	19.40	20.60	27.90	18.20
Co	17.90	27.30	24.80	18.10	21.80	17.90	16.00	16.80	17.20	13.90
V	5	113	131	80	65	34	42	31	34	44
La	19.1	19	23.4	17.7	35.2	16.6	21.5	26.4	14.5	15.6
Ce	36.7	39.9	44.7	36	72.2	31.7	43.6	53.1	32.6	32.5
Pr	4.75	4.81	5.48	4.55	8.81	4.12	5.33	6.39	4.17	4.3
Nd	19.9	19.1	23.4	18.6	36.6	16.3	20.3	26.1	18.7	19.3
Sm	4.78	4.76	5.19	4.35	8.26	4.24	5.01	6.09	4.52	4.43
Eu	1.65	1.67	2.21	1.53	3.19	1.63	2.33	2	1.49	1.63
Gd	5.35	5.3	5.48	4.76	9.07	4.66	5.88	6.77	5.31	5.15
Tb	0.79	0.8	0.8	0.72	1.32	0.72	0.81	1.04	0.81	0.8
Dy	4.43	4.69	4.44	5.06	8.05	4.32	4.61	6.19	4.86	5.16
Ho	0.88	1	0.85	0.89	1.49	0.84	0.87	1.29	0.91	1.07
Er	2.79	2.63	2.48	2.4	3.96	2.44	2.39	3.85	2.87	2.98
Tm	0.34	0.36	0.33	0.34	0.49	0.33	0.32	0.51	0.4	0.41
Yb	2.22	2.09	2.01	2.21	3.17	1.98	1.84	3.44	2.76	2.72
Lu	0.31	0.34	0.29	0.29	0.43	0.32	0.28	0.51	0.39	0.41
∑REE	103.99	106.45	121.06	99.40	192.24	90.20	115.07	143.68	94.29	96.46
Nb/Y	0.75	0.63	0.83	0.56	0.73	0.65	0.65	0.62	0.43	0.43
Zr/Nb	7.82	9.18	7.05	9.19	7.24	9.19	8.20	9.29	13.63	13.37
K/Nb	415.9	538.7	1216.3	536.2	262.29	403.3	636.7	368.9	675.8	658.5
Ba/Nb	8.40	11.02	15.22	11.51	6.23	7.54	19.61	10.51	9.30	9.75
La/Nb	1.06	1.14	1.14	1.16	1.29	1.17	1.41	1.22	1.26	1.31
Ce/Ce*	2.38	1.02	0.93	0.97	0.98	0.93	1.00	0.98	1.00	0.94

*2Major elements determined by XRF in Naruto University, Japan; and trace elements by ICP-MS in ACME laboratory, Canada reported in Deevsalar *et al.* (2014).

Ce/Ce* is calculated by $Ce_{CN}/La_{CN}{}^{2/3}\times Nd_{CN}{}^{1/3}$.

Table 2
Sr-Nd isotopic composition of the mafic-intermediate dykes from MBPC.

	$^{87}Sr/^{86}Sr$ (measured)	Rb (ppm)	Sr (ppm)	Error $\times 10^{-6}$	$^{87}Sr/^{86}Sr$ (initial)	$^{143}Nd/^{144}Nd$ (measured)	Sm (ppm)	Nd (ppm)	$^{143}Nd/^{144}Nd$ (initial)	$\varepsilon_{Nd}(T)$	Error $\times 10^{-6}$
Group-1 ~ 168 Ma											
BR02	0.72948	216.1	93.1	6	0.71362	0.51216	7.03	38.28	0.51204	-7.54	4
BR07	0.72464	141.6	89.22	6	0.71329	0.51218	7.13	37.15	0.51206	-7.18	6
MN2a	0.70831	34.7	82.7	7	0.70770	0.51228	5.98	25.38	0.51212	-5.86	15
MN8	0.72679	147	83.52	6	0.71427	0.51223	6.25	33.60	0.51211	-6.10	5
BR03b	0.72560	151	98.52	6	0.71510	0.51214	6.691	37.43	0.51202	-7.92	3
Group-2 ~ 42 Ma											
M38	0.70712	13.7	464.0	7	0.70707	0.51281	27.71	34.90	0.51268	1.8	6
M22	0.70546	22.5	450.4	7	0.70537	0.51273	39.80	55.89	0.51261	0.6	5
BR04	0.70551	34.1	424.1	6	0.70538	0.51279	29.54	40.04	0.51267	1.6	7
M50	0.70780	118	427.2	6	0.70732	0.51278	33.92	50.11	0.51267	1.7	5
M25b	0.70503	17.9	524.8	8	0.70498	0.51279	28.43	39.83	0.51267	1.7	6
M33	0.70754	40.1	625.0	7	0.70743	0.51273	34.25	53.96	0.51262	0.8	4
MN7	0.70602	29.79	89.22	6	0.70591	0.51280	4.80	19.06	0.51276	3.5	5
M29	0.70500	17.64	482.5	6	0.70494	0.51279	5.63	23.87	0.51275	3.3	10

Table 3
Lead isotope composition of the mafic-intermediate dykes from MBPC.

	$^{206}Pb/^{204}Pb$ (measured)	$^{207}Pb/^{204}Pb$ (measured)	$^{208}Pb/^{204}Pb$ (measured)	U	Th	Pb	$^{206}Pb/^{204}Pb(i)$	$^{207}Pb/^{204}Pb(i)$	$^{208}Pb/^{204}Pb(i)$
Group-1 ~ 168 Ma									
BR02	18.76	15.69	39.56	1.41	6.75	14.36	18.44	15.68	38.57
BR07	18.58	15.65	38.96	2.01	15.68	22.04	18.43	15.64	38.58
MN2a	18.79	15.70	39.03	1.41	6.75	14.36	18.63	15.70	38.78
MN8	18.57	15.64	38.84	1.93	14.07	22.42	18.43	15.63	38.51
BR03b	18.55	15.68	38.97	1.6	16.55	28.35	18.46	15.68	38.66
Group-2 ~ 42 Ma									
M38	18.46	15.65	38.69	0.3	1.3	2.76	18.417	15.645	38.629
M22	18.46	15.59	38.61	0.7	2.5	1.38	18.251	15.583	38.373
BR04	18.53	15.66	38.75	0.3	1.3	1.49	18.447	15.654	38.636
M50	18.60	15.65	38.89	0.6	1.9	11.29	18.578	15.650	38.869
M33	18.71	15.67	38.98	0.9	4.5	1.87	18.519	15.662	38.657
M29a	18.44	15.63	38.65	0.36	1.66	10.83	18.425	15.634	38.633
MN13	18.73	15.67	38.93	0.34	1.41	3.63	18.693	15.664	38.875
MN12	18.77	15.67	38.97	0.48	2.12	3.76	18.713	15.664	38.899
MN4	18.48	15.66	38.74	0.30	1.41	7.75	18.468	15.658	38.719
MN7	18.68	15.67	38.84	0.31	1.43	5.74	18.654	15.668	38.809
	Standard Sample: Mean (n=20)								
	16.9437	15.5010	36.7236						
	2SD								
	0.0023	0.0028	0.0053						

Table 4
The results of melting and mixing model calculations for Middle Jurassic gabbro-dioritic dykes.

	Mantle wedge				High crustal level					
	Source	Mixing		NMBM*4	Modal Fractional Melting			AFC	Mixing and FC	
	PM*1	A*2	EM*3	f_m= 0.15*5	Source	Melting parameter		f_c*8 = 0.4; R*9 = 0.3	Mixing*10	FC*11
					Greywacke*6	Kd*7	f_m= 0.25		f_{mix}= 0.4	f_c= 0.6
Rb	0.63	71.04	4.16	27.28	72	1.43	54.87	110.83	37.90	62.20
Ba	6.99	1019.20	57.60	379.26	426	2.34	214.48	1082.61	310.23	490.64
Th	0.09	5.10	0.34	2.22	9	0.10	7.17	11.07	6.35	10.46
U	0.02	1.11	0.08	0.50	2	0.05	0.14	2.51	0.50	0.84
Nb	0.71	4.64	0.91	6.01	8.4	1.42	6.44	20.31	6.13	10.20
K	249.98	21038.38	1289.40	8164.83	16602.8	0.87	18301.9	29504.28	12291.53	20001.93
La	0.69	16.72	1.49	9.44	34	0.16	47.62	13.18	32.19	27.13
Ce	1.77	34.55	3.41	20.76	58	0.16	78.69	22.60	57.01	45.69
Pr	0.28	1.64	0.34	2.01	6.1	0.12	6.25	1.63	5.20	3.29
Sr	21.10	473.80	43.73	264.40	201	0.96	206.88	384.42	241.61	295.96
P	94.98	486.66	114.56	654.94	567.3		-	1978.63	-	
Nd	1.35	15.51	2.06	11.41	25	0.14	29.83	5.30	24.76	12.36
Zr	11.20	254.15	23.35	129.59	302	0.06	68.68	465.25	148.81	235.87
Sm	0.44	2.79	0.56	2.77	4.6	0.14	5.75	0.76	5.05	1.94
Eu	0.17	0.61	0.19	0.90	1.2	0.60	1.65	0.19	1.23	0.43
Ti	1300.24	1922.51	1331.36	5682.87	4315.17	0.02	0.27	15382.34	3411.99	5455.17
Dy	0.74	1.60	0.78	3.11	3.4	0.17	4.88	0.73	4.55	1.96
Y	4.55	8.81	4.77	15.10	26	0.77	31.05	38.16	21.73	30.79
Yb	0.49	0.72	0.50	1.34	2.1	0.16	2.93	1.10	2.44	2.02
Lu	0.07	0.10	0.08	0.18	0.37	0.16	0.51	0.21	0.40	0.36

*1 PM: primitive mantle composition (Sun & McDonough 1989)
*2 Subduction sediment-derived fluids/melts: 0.55SF/0.45SM. The parameters used in modeling are: normalizing values from Sun & McDonough (1989), Bulk subducted sediment composition (BOS) are from Plank & Langmuir (1998), sediment fluid partition coefficients (DSF) from Johnson & Plank (1999). Sediment melt (SM) calculated by 5% modal fractional melting of bulk subducted sediment, sediment fluids (SF) composition calculated using BOS and DSF($C_{BOS/DSF}$).
*3 Middle Jurassic Enriched Mantle (80% PM + 20% A)
*4 NMBM: Non-Modal Batch Melting (Mode-I, Supplementary item 3, Table S3)
*5 f_m: degree of melting = 15%; partial melting of metasomatised garnet-spinel Lherzolite (Supplementary Item 3, Table S3)
*6 Upper crust-greywacke composition is from Wedepohl (1995)
*7 Bulk partition coefficient calculated for greywacke (35%Qtz + 30%Bio + 15% Plg + 5% AF+ 15% Mus)
*8 F_c: degree of fractional crystallization; Bulk partition coefficient calculated for 70.66% Cpx + 26.77% Pl + 0.44% Ap
*9 R-value: EM/UCC-greywacke
*10 Mixing of EM and Greywacke-melt. f_{mix}: degree of mixing
*11 Fractional crystallization of 70.66% Cpx + 26.77% Pl + 0.44% Ap from crustally-contaminated EM

Table 5

The results of melting, mixing and fractional crystallization model calculations for Late Eocene gabbroic dykes.

	Source region					Crustal level
	Source	NMBM*[2]			Mixing*[6]	Fractional crystallization
		Mode-II	Mode-III	Mode-IV		
	PM*[1]	$F_{melting}$ = 0.05*[3]	$F_{melting}$ = 0.05*[4]	$F_{melting}$ = 0.15*[4]	Grt Lhz Melt$_{(5\%)}$ + Spl Lhz Melt$_{(15\%)}$	Residual melt*[7] F= 0.45
Rb	0.63	12.39	12.40	4.20	7.48	16.59
Ba	6.99	136.61	136.74	46.29	82.47	182.71
Th	0.09	1.67	1.66	0.56	1.00	2.17
U	0.02	0.41	0.41	0.14	0.25	0.55
Nb	0.71	14.05	14.06	4.74	8.47	18.79
K	249.98	4908.51	4902.47	1659.08	2956.44	6517.45
La	0.69	12.50	12.41	4.48	7.65	14.99
Ce	1.77	30.00	29.68	11.34	18.68	35.84
Pr	0.28	5.27	5.23	1.82	3.19	5.80
Sr	21.10	347.09	342.83	133.91	217.48	468.20
P	94.98	1268.97	1255.22	549.71	831.91	1842.80
Nd	1.35	18.64	18.18	8.17	12.17	20.96
Zr	11.20	161.90	157.07	69.41	104.48	222.93
Sm	0.44	4.68	4.43	2.49	3.27	5.22
Eu	0.17	2.62	2.40	1.10	1.62	2.57
Ti	1300.24	11573.47	11427.96	6672.09	8574.44	18366.38
Dy	0.74	3.19	2.50	3.79	3.27	5.22
Y	4.55	18.35	14.32	22.89	19.46	37.54
Yb	0.49	1.16	0.84	2.47	1.82	3.29
Lu	0.07	0.14	0.10	0.34	0.24	0.46

*[1] PM: primitive mantle composition (Sun & McDonough 1989)
*[2] NMBM: Non-Modal Batch Melting
*[3] 5% partial melting of Garnet-Spinel Lherzolite (Mode-II, Supplementary Item 3, Table S2, S3)
*[4] 5% partial melting of Garnet Lherzolite (Mode-III, Supplementary Item 3, Table S2, S3)
*[5] 15% partial melting of Spinel Lherzolite (Mode-IV, Supplementary Item 3, Table S2, S3)
*[6] EM: mixing between melts originated from garnet lherzolite and spinel lherzolite source
*[7] Residual melt of fractional crystallization of 0.5 Ol + 0.35 Cpx + 0.1 Am ± 0.05 Apt from enriched mantle magma

Figure

Fig. 1

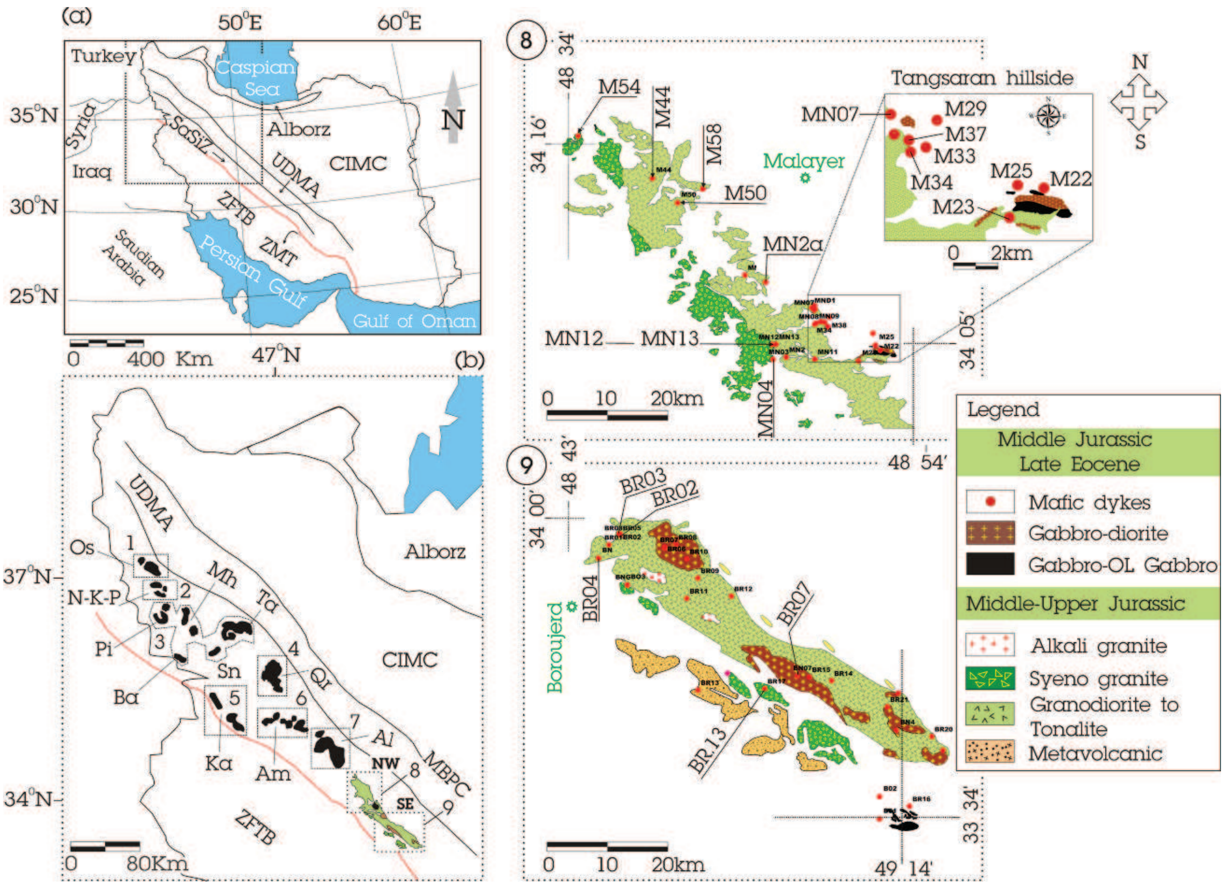
(a)
50°E
60°E
Turkey
Caspian Sea
Syria
Iraq
SaSiZ
Alborz
UDMA
CIMC
ZFTB
ZMT
Saudian Arabia
Persian Gulf
Gulf of Oman
35°N
30°N
25°N
0 400 Km
47°N
(b)
UDMA
Alborz
CIMC
MBPC
ZFTB
Os
N-K-P
Pi
Ba
Mh
Ta
Sn
Qr
Ka
Am
Al
NW
SE
37°N
34°N
0 80Km
Tangsaran hillside
M54
M44
M58
M50
MN07
M29
M37
M33
M34
M25
M22
M23
Malayer
MN2a
MN12
MN13
MN04
0 2km
0 10 20km
Legend
Middle Jurassic Late Eocene
Mafic dykes
Gabbro-diorite
Gabbro-OL Gabbro
Middle-Upper Jurassic
Alkali granite
Syeno granite
Granodiorite to Tonalite
Metavolcanic
BR03
BR02
BR04
BR07
BR13
Boroujerd
0 10 20km
N
S

Fig. 2

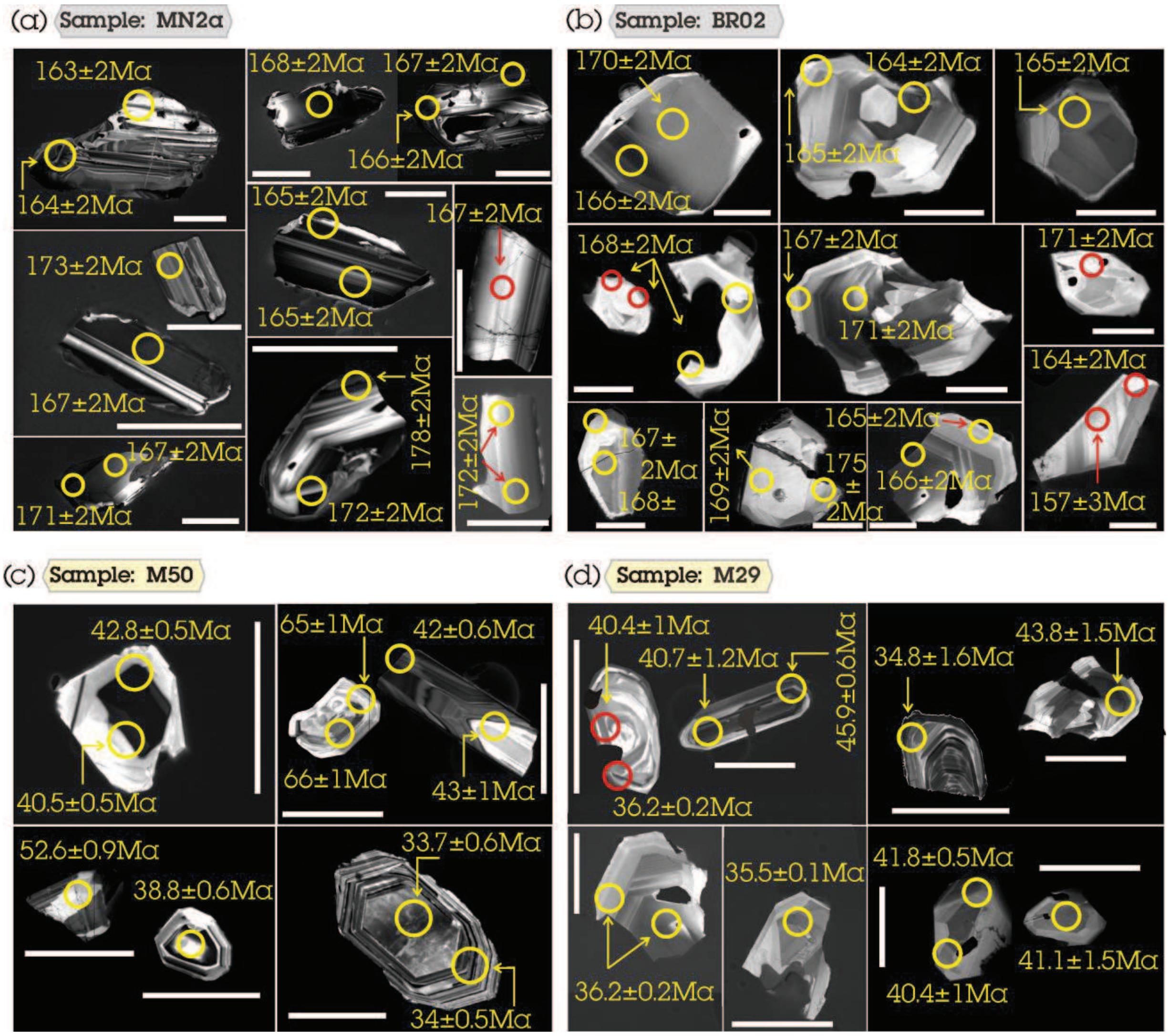

Fig. 3

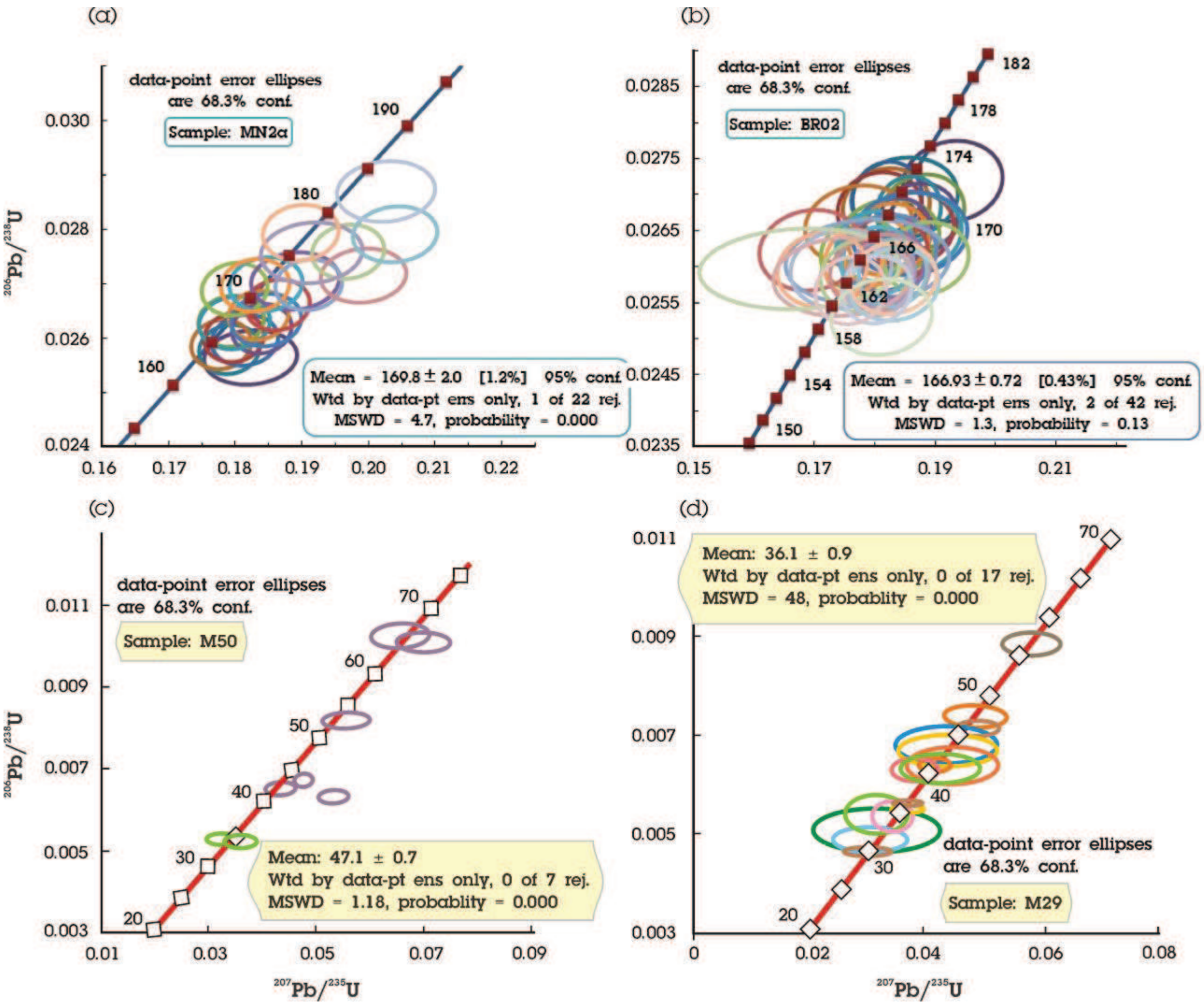
(a)
data-point error ellipses are 68.3% conf.
Sample: MN2a
Mean = 169.8 ± 2.0 [1.2%] 95% conf.
Wtd by data-pt errs only, 1 of 22 rej.
MSWD = 4.7, probability = 0.000
(b)
data-point error ellipses are 68.3% conf.
Sample: BR02
Mean = 166.93 ± 0.72 [0.43%] 95% conf.
Wtd by data-pt errs only, 2 of 42 rej.
MSWD = 1.3, probability = 0.13
(c)
data-point error ellipses are 68.3% conf.
Sample: M50
Mean: 47.1 ± 0.7
Wtd by data-pt errs only, 0 of 7 rej.
MSWD = 1.18, probablity = 0.000
(d)
Mean: 36.1 ± 0.9
Wtd by data-pt errs only, 0 of 17 rej.
MSWD = 48, probablity = 0.000
data-point error ellipses are 68.3% conf.
Sample: M29
206Pb/238U
207Pb/235U

Fig. 4

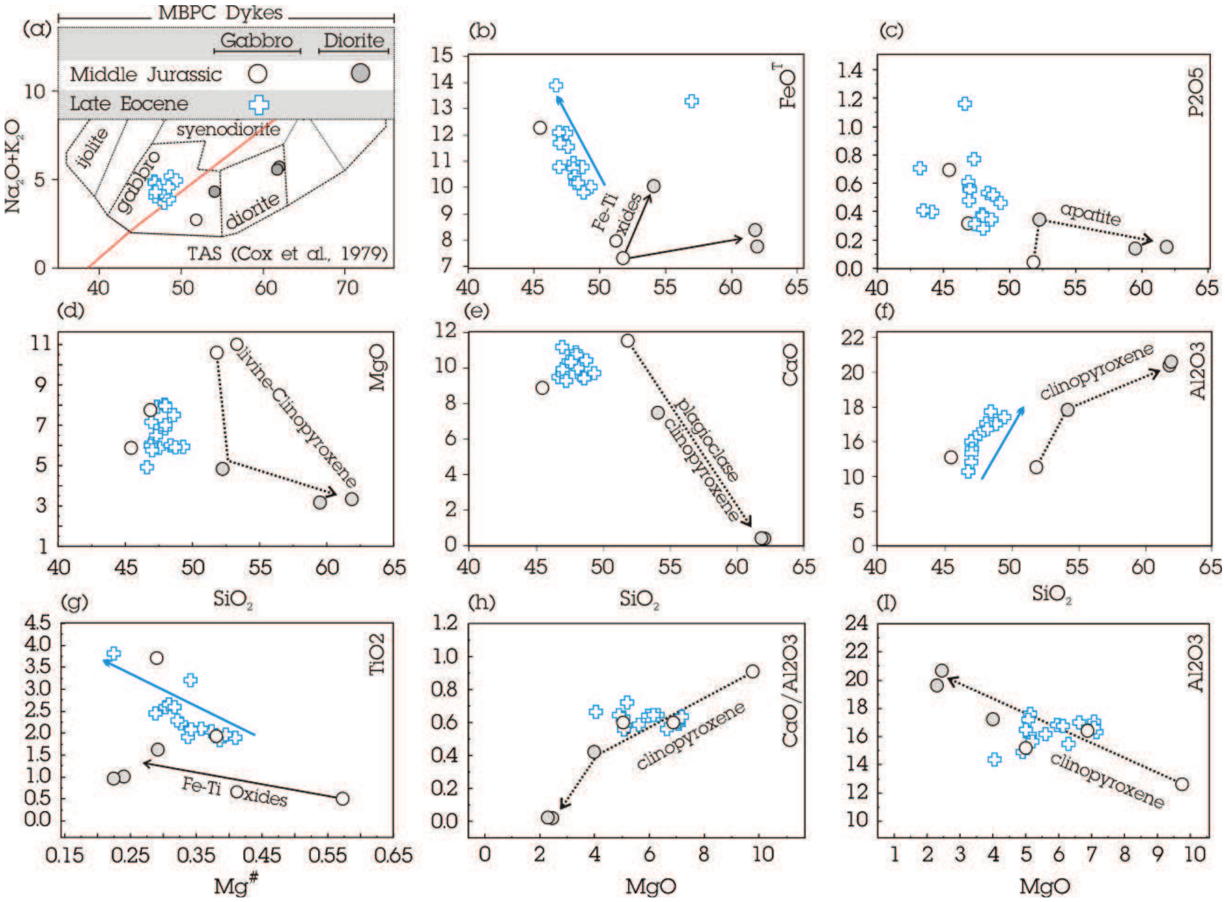
(a)
MBPC Dykes
Gabbro
Diorite
Middle Jurassic
Late Eocene
ijolite
syenodiorite
gabbro
diorite
TAS (Cox et al., 1979)
Na_2O+K_2O
(b)
FeO^T
Fe-Ti Oxides
(c)
P2O5
apatite
(d)
MgO
Olivine-Clinopyroxene
SiO$_2$
(e)
CaO
plagioclase
clinopyroxene
SiO$_2$
(f)
Al2O3
clinopyroxene
SiO$_2$
(g)
TiO2
Fe-Ti Oxides
Mg$^\#$
(h)
CaO/Al2O3
clinopyroxene
MgO
(I)
Al2O3
clinopyroxene
MgO

Fig. 5

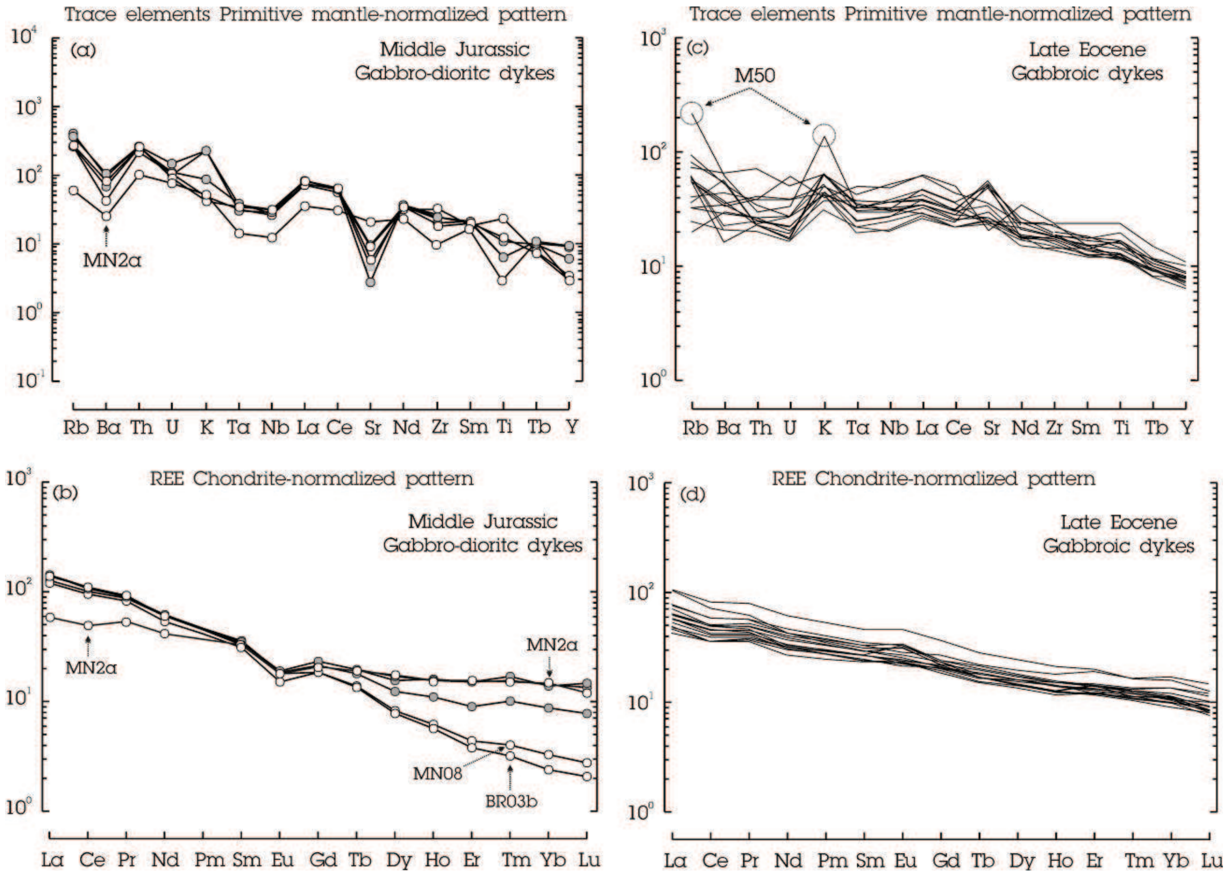

Trace elements Primitive mantle-normalized pattern
(a)
Middle Jurassic
Gabbro-dioritc dykes
MN2a
Rb Ba Th U K Ta Nb La Ce Sr Nd Zr Sm Ti Tb Y
Trace elements Primitive mantle-normalized pattern
(c)
Late Eocene
Gabbroic dykes
M50
Rb Ba Th U K Ta Nb La Ce Sr Nd Zr Sm Ti Tb Y
REE Chondrite-normalized pattern
(b)
Middle Jurassic
Gabbro-dioritc dykes
MN2a
MN2a
MN08
BR03b
La Ce Pr Nd Pm Sm Eu Gd Tb Dy Ho Er Tm Yb Lu
REE Chondrite-normalized pattern
(d)
Late Eocene
Gabbroic dykes
La Ce Pr Nd Pm Sm Eu Gd Tb Dy Ho Er Tm Yb Lu

Fig. 6

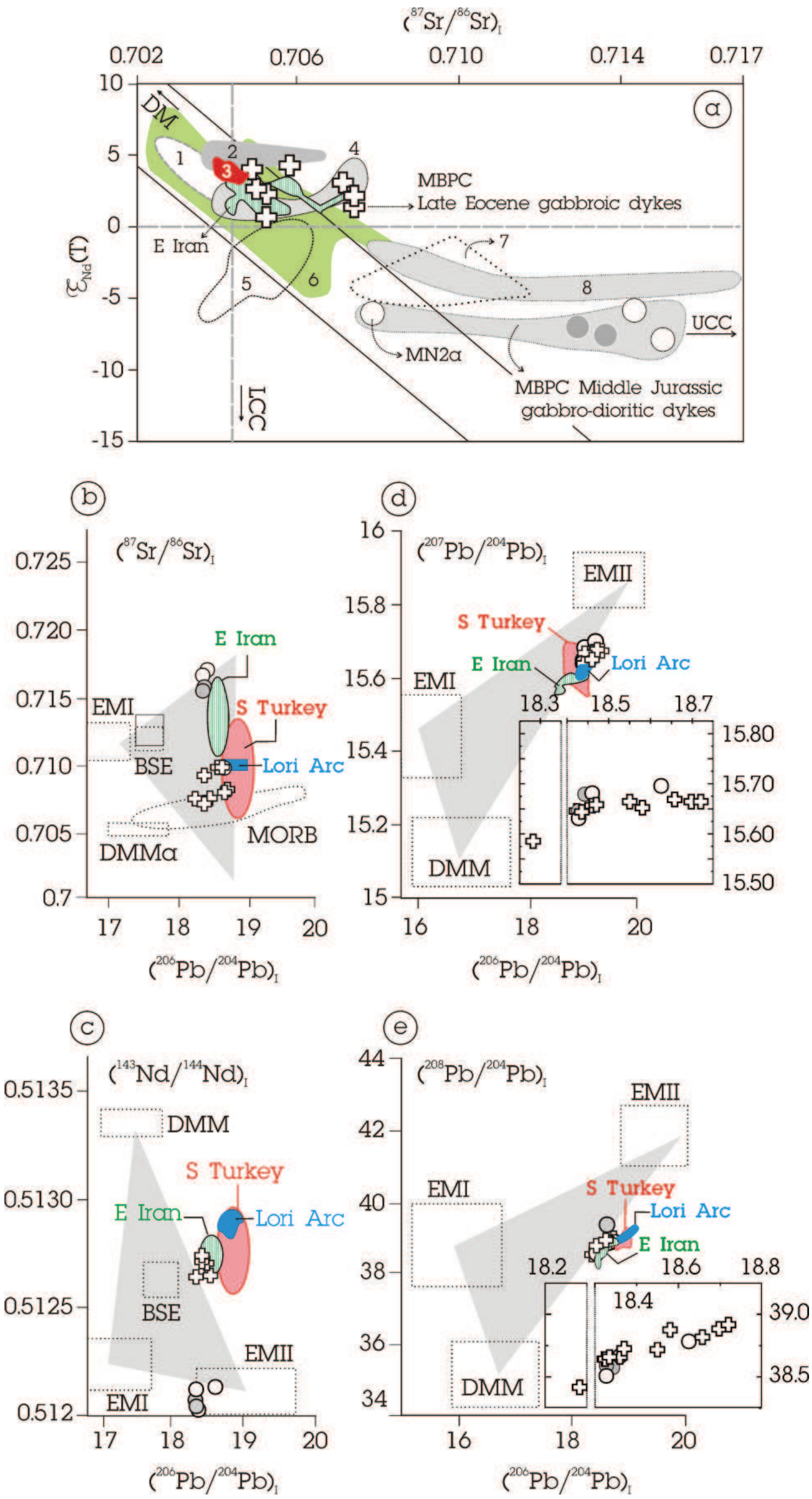

($^{87}Sr/^{86}Sr)_I$
0.702 0.706 0.710 0.714 0.717
10 5 0 -5 -10 -15
$\varepsilon_{Nd}(T)$
a
DM
1 2 3 4 5 6 7 8
MBPC
Late Eocene gabbroic dykes
E Iran
UCC
MN2a
MBPC Middle Jurassic
gabbro-dioritic dykes
LCC
b
($^{87}Sr/^{86}Sr)_I$
0.725 0.720 0.715 0.710 0.705 0.7
E Iran
S Turkey
Lori Arc
EMI
BSE
MORB
DMMa
17 18 19 20
($^{206}Pb/^{204}Pb)_I$
d
($^{207}Pb/^{204}Pb)_I$
16 15.8 15.6 15.4 15.2 15
EMII
S Turkey
E Iran
Lori Arc
EMI
DMM
18.3 18.5 18.7
15.80 15.70 15.60 15.50
16 18 20
($^{206}Pb/^{204}Pb)_I$
c
($^{143}Nd/^{144}Nd)_I$
0.5135 0.5130 0.5125 0.512
DMM
S Turkey
E Iran
Lori Arc
BSE
EMII
EMI
17 18 19 20
($^{206}Pb/^{204}Pb)_I$
e
($^{208}Pb/^{204}Pb)_I$
44 42 40 38 36 34
EMII
EMI
S Turkey
Lori Arc
E Iran
18.2 18.6 18.8
18.4
39.0 38.5
DMM
16 18 20
($^{206}Pb/^{204}Pb)_I$

Fig. 7

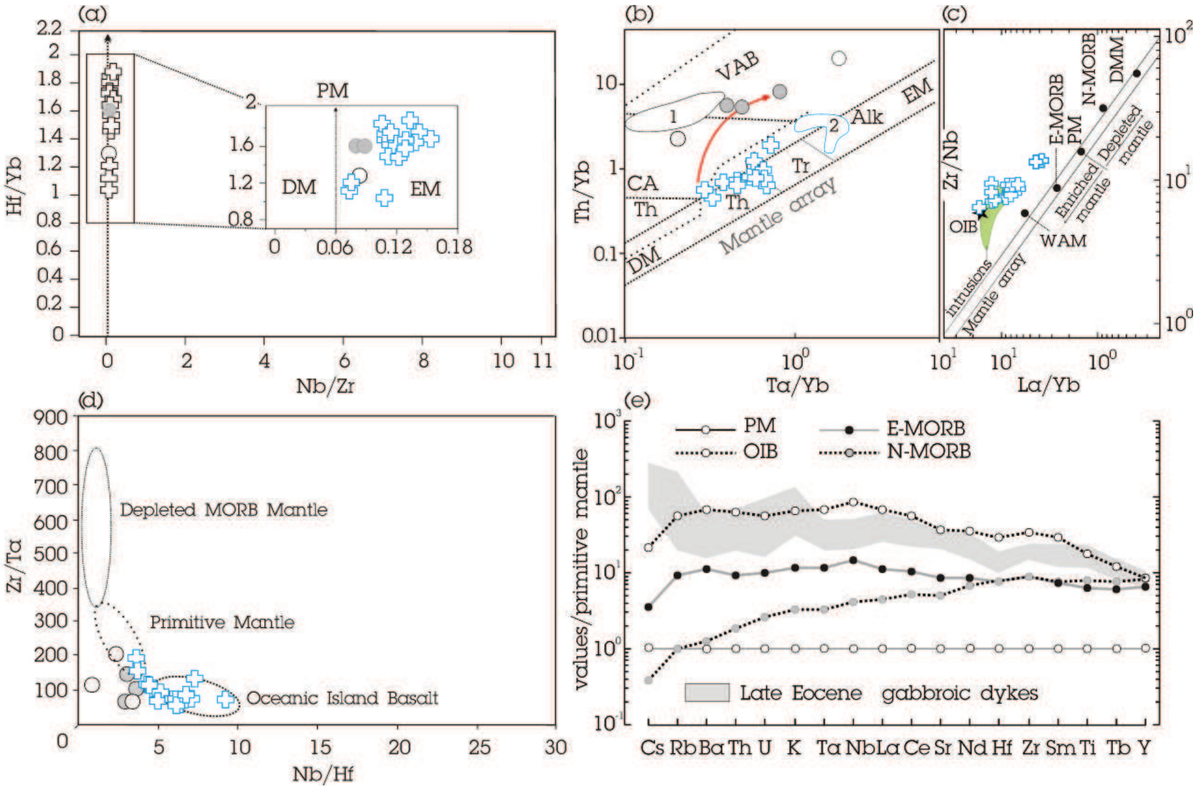

(a)
Hf/Yb
Nb/Zr
PM
DM
EM
(b)
VAB
Th/Yb
Ta/Yb
CA
Th
Alk
Tr
EM
DM
Mantle array
(c)
Zr/Nb
La/Yb
OIB
intrusions
Mantle array
WAM
E-MORB
PM
N-MORB
DMM
Enriched mantle
Depleted mantle
(d)
Zr/Ta
Nb/Hf
Depleted MORB Mantle
Primitive Mantle
Oceanic Island Basalt
(e)
PM
OIB
E-MORB
N-MORB
values/primitive mantle
Late Eocene gabbroic dykes
Cs Rb Ba Th U K Ta Nb La Ce Sr Nd Hf Zr Sm Ti Tb Y

Fig. 8

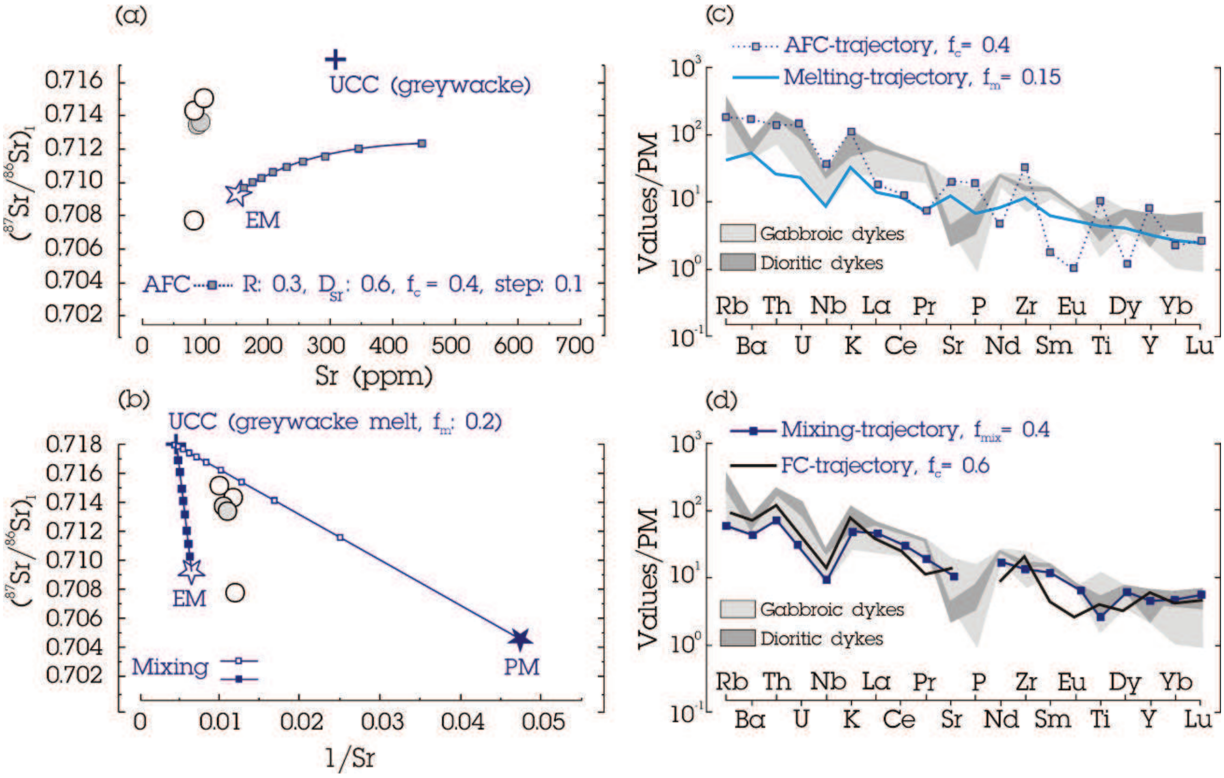
(a)
UCC (greywacke)
EM
AFC R: 0.3, D_Sr: 0.6, f_c = 0.4, step: 0.1
(87Sr/86Sr)i
Sr (ppm)
(b)
UCC (greywacke melt, f_m: 0.2)
EM
PM
Mixing
(87Sr/86Sr)i
1/Sr
(c)
AFC-trajectory, f_c= 0.4
Melting-trajectory, f_m= 0.15
Gabbroic dykes
Dioritic dykes
Values/PM
Rb Th Nb La Pr P Zr Eu Dy Yb
Ba U K Ce Sr Nd Sm Ti Y Lu
(d)
Mixing-trajectory, f_mix= 0.4
FC-trajectory, f_c= 0.6
Gabbroic dykes
Dioritic dykes
Values/PM
Rb Th Nb La Pr P Zr Eu Dy Yb
Ba U K Ce Sr Nd Sm Ti Y Lu

Fig. 9

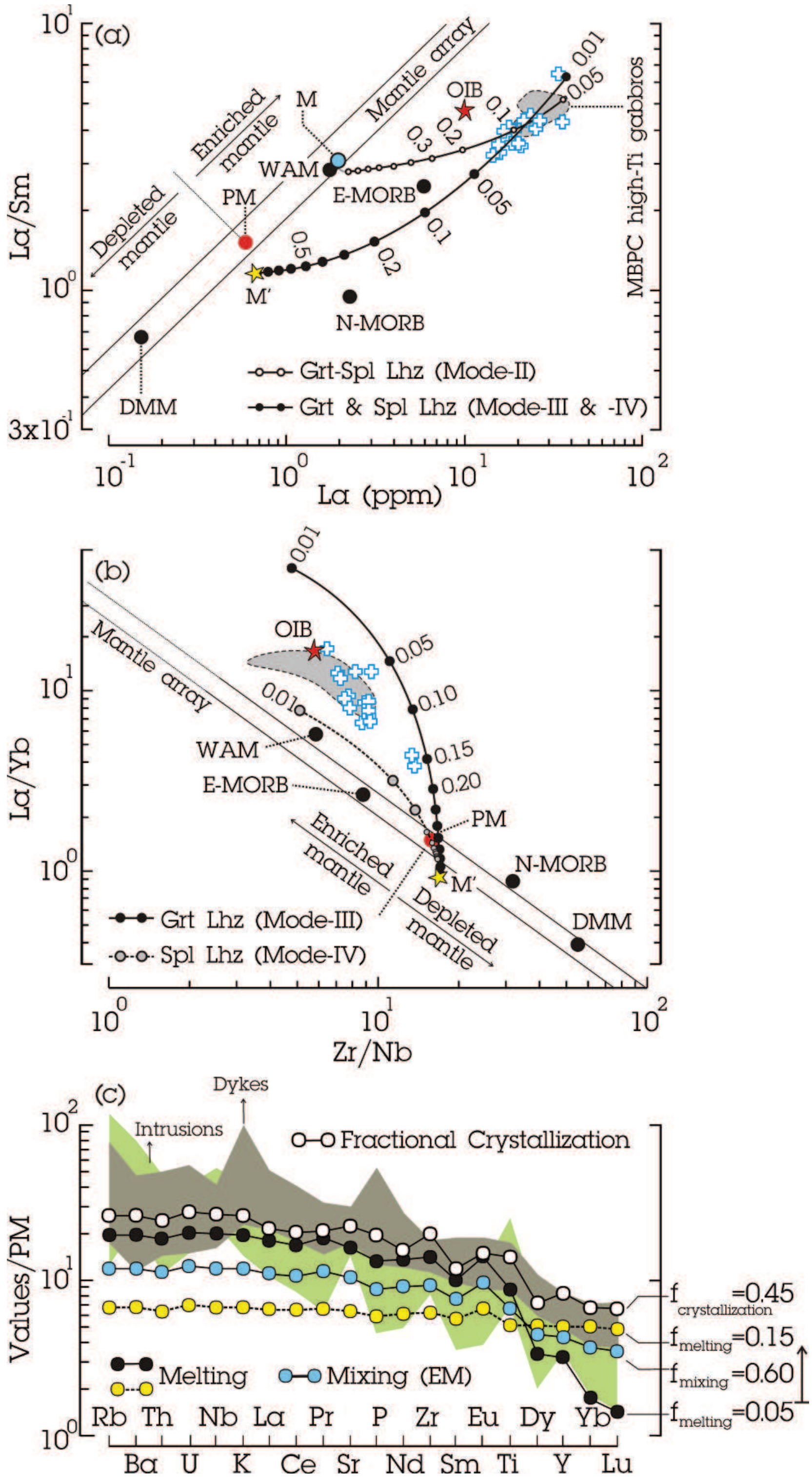

(a)
La/Sm
La (ppm)
Depleted mantle
Enriched mantle
Mantle array
M
OIB
WAM
PM
E-MORB
M'
N-MORB
DMM
MBPC high-Ti gabbros
Grt-Spl Lhz (Mode-II)
Grt & Spl Lhz (Mode-III & -IV)
(b)
La/Yb
Zr/Nb
Mantle array
OIB
WAM
E-MORB
PM
N-MORB
DMM
M'
Enriched mantle
Depleted mantle
Grt Lhz (Mode-III)
Spl Lhz (Mode-IV)
(c)
Values/PM
Dykes
Intrusions
Fractional Crystallization
Melting
Mixing (EM)
$f_{crystallization}$=0.45
$f_{melting}$=0.15
f_{mixing}=0.60
$f_{melting}$=0.05
Rb Th Nb La Pr P Zr Eu Dy Yb
Ba U K Ce Sr Nd Sm Ti Y Lu

Fig. 10

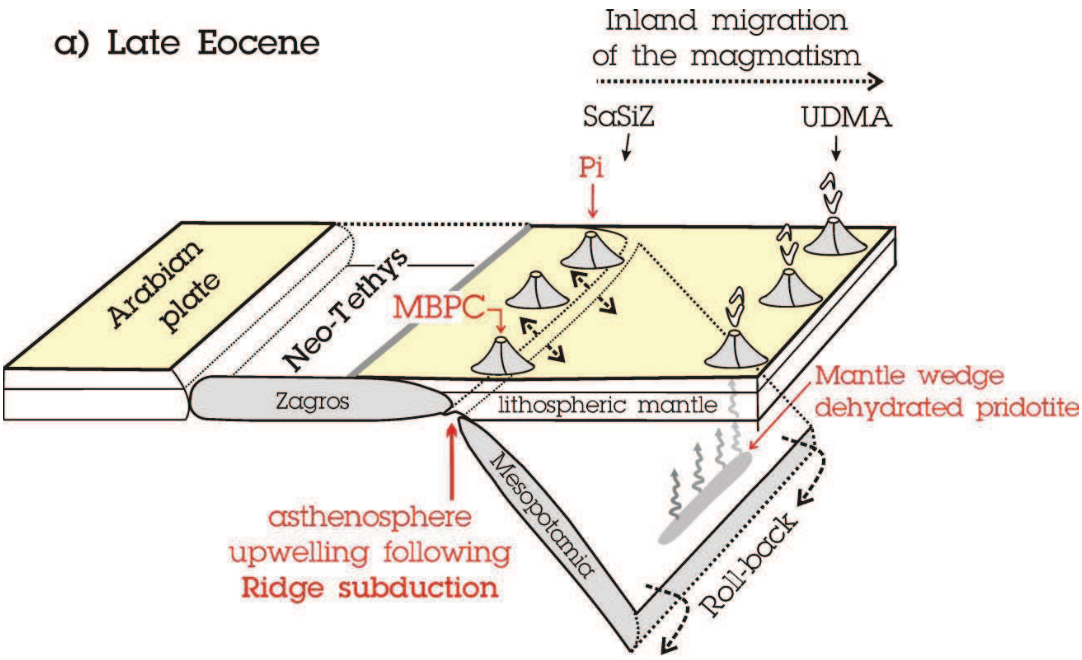

a) Late Eocene
Inland migration
of the magmatism
SaSiZ
UDMA
Pi
Arabian plate
Neo-Tethys
MBPC
Zagros
lithospheric mantle
Mantle wedge
dehydrated pridotite
asthenosphere
upwelling following
Ridge subduction
Mesopotamia
Roll-back

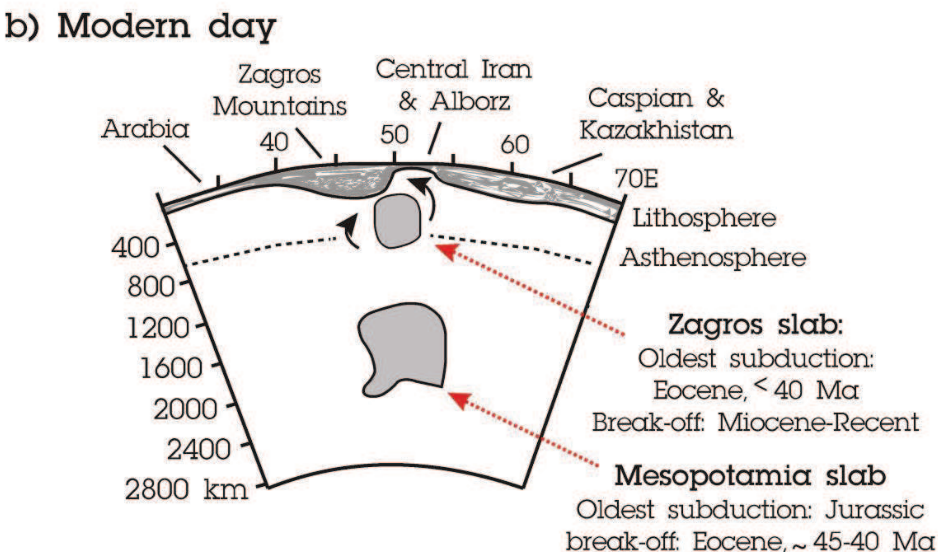

b) Modern day
Zagros
Mountains
Central Iran
& Alborz
Caspian &
Kazakhistan
Arabia
40
50
60
70E
Lithosphere
Asthenosphere
400
800
1200
1600
2000
2400
2800 km
Zagros slab:
Oldest subduction:
Eocene, < 40 Ma
Break-off: Miocene-Recent
Mesopotamia slab
Oldest subduction: Jurassic
break-off: Eocene, ~ 45-40 Ma

FIGURE CAPTIONS:

Fig. 1 (a) Simplified distribution of the main tectonic subdivisions of Iran. (b) Distribution of magmatic complexes in the N-SaSZ and the position of the MBPC. The MBPC is marked by two rectangles (8 and 9). 1- Oshnavieh (Os); Urumieh; 2- Naghade-Khalfe-Pasveh (N-K-P); 3- Piranshahr (Pi), Saqez, Takab (Ta); Miandoab, Mahabad (Mh); Sanandaj (Sn) and Baneh (Ba); 4- Qorveh (Qr); 5- Kamyaran (Ka); 6- Almogholagh (Al); 7- Alvand (Al), 8- Malayer (Ma); 9- Boroujerd (Br). (c) The areas marked by (8) and (9) respectively contain geological maps of the MBPC indicating the distribution of mafic–intermediate dykes. The locations of dyke samples with corresponding geochemical data are labelled.

Fig. 2 Representative CL images of zircon grains.

Fig. 3 Conventional U–Pb concordia plots (Tera and Wasserburg, 1972) and weighted mean zircon ages for MBPC magmatic dykes. (a) Middle Jurassic diorite. (b) Middle Jurassic gabbro. (c, d) Late Eocene gabbro.

Fig. 4 (a-f) Harker diagrams of major oxides (wt. %) vs. SiO_2 (wt. %) for the gabbro–dioritic dykes from the MBPC. Arrows indicate changes in composition relative to magma evolution. Thin dashed and solid lines are respectively mineral fractionation and accumulation vectors from an assumed parental magma (MN_{2a}). (g-i) TiO_2 (wt. %) vs. $Mg^{\#}$, CaO/Al_2O_3 and Al_2O_3 vs. MgO (wt. %).

Fig. 5 (a, b) Primitive Mantle (PM)-normalised trace element diagrams and Chondrite-normalised REE patterns for for the Middle Jurassic dykes, (c, d) PM-normalised trace element diagrams and Chondrite-normalized REE patterns for Late Eocene gabbroic dykes. PM compositions are from Taylor and McLennan (1985). Chondrite compositions are from Nakamura (1974).

Fig. 6 Isotope ratio diagrams for the MBPC dykes. (a) $(^{87}Sr/^{86}Sr)_i$ vs. εNd. 1- Hawaii (PREMA): (Hofmann 2005); 2- Upper Jurassic – Lower Cretaceous Kapan arc (Mederer *et al.* 2013); 3- Late Cenozoic Georgian and NW Armenian mafic alkaline rocks (Neill *et al.* 2013, 2015); 4- MBPC

Late Eocene gabbroic intrusions (Deevsalar *et al.* 2017); 5- MBPC Middle Jurassic gabbroic intrusions (Deevsalar *et al.* 2017); 6- OIB (Zhang *et al.* 2002); 7- MBPC granitoids (Ahmadi-Khalaji *et al.* 2006; Ahadnejad *et al.* 2010; 2011); 8- Alvand granite (Shahbazi *et al.* 2010; Sepahi *et al.* 2017). (b, c) Initial Sr and Nd isotopic values plotted against $^{206}Pb/^{204}Pb$. (d, e) $^{206}Pb/^{204}Pb$ vs. $^{207}Pb/^{204}Pb$ and $^{208}Pb/^{204}Pb$ for the MBPC dykes. Labelled rectangular fields in each plot show mantle reservoirs (EMI, EMII, HIMU, and DMM) taken from Shimuda (2009). Also shown are Late Cenozoic lavas from Karacadag, S Turkey (Ekici *et al.* 2014) and E Iran (Kheirkhah *et al.* 2015); Upper Jurassic-Lower Cretacous mafic rocks from the Kapan Arc (Mederer *et al.* 2013); and Late Cenozoic mafic lavas of NE Armenia (Neill *et al.* 2015). The gray triangles are used for screening the proportion of each of these mantle reservoirs in the source region.

Fig. 7 (a) Hf/Yb vs. Nb/Zr plot (John *et al.* 2004). PM: primitive mantle, EM: enriched mantle, DM: depleted mantle. (b) Th/Yb vs. Ta/Yb plot (Pearce 1983). Enclosed area in this figure: 1- Upper Jurassic- Late Cretaceous rocks from the Kapan arc (Mederer *et al.* 2013), 2- alkaline rocks from East Iran (Kheirkhah *et al.* 2015). VAB: volcanic arc basalts, Th; tholeiitic, Alk: alkaline, Tr: transitional, CA; calc-alkaline. (c) La/Yb vs. Zr/Nb (Aldanmaz *et al.* 2006). WAM (Western Anatolian Mantle); (d) Ta/Zr vs. Nb/Hf. Green filed shows the MBPC Late Eocene Gabbros (Deevsalar *et al*. 2017). (e) Comparison of the concentration of selected trace elements in the Late Eocene gabbroic dykes with E-MORB, N-MORB and OIB (values from Sun & McDonough 1989).

Fig. 8 Trace element modelling of magmatic processes for Group-1 dykes. (a) AFC trajectory on a $(^{87}Sr/^{86}Sr)_i$ vs. Sr (ppm) plot. Parameters are R: 0.3, D_{Sr}: 0.6, and contaminant is upper crusta-greywacke (taken from Wedepohl 1995; 35% Qtz + 30% Bio + 15% Plg + 5% Alk + 15% Mus). AFC calculated using the equations of DePaolo (1981). (b) Mixing model trajectory plotted on $(^{87}Sr/^{86}Sr)_i$ vs. 1/Sr (ppm). End-members are metasomatised mantle-derived magma (Supplementary Item 1, Table S4) and greywacke-derived melt (modal fractional melting of upper crustal-greywacke, Table 5; $F_{melting}$: 0.2). The degree of mixing (F_{mixing}) is 0.4. Each point on the curves represents 10% assimilation. Mixing equation is from Langmuir *et al.* 1978. PM-normalized trace element pattern of: (c) metasomatically-enriched mantle magma ($F_{melting}$: 15%) and AFC-trajectory, and (d) mixing and FC model trajectories modelled on a multi-element plot of Group-1 dykes. Parameters for non-modal batch melting and Rayleigh fractional crystallization (FC) are given in Supplementary Item 3, Tables S2 and S3.

Fig. 9 Non-modal batch melting vectors are plotted on (a) La/Sm vs. La (ppm), and (b) Zr/Nb vs. La/Yb logarithmic plots for Group-2 dykes. M: enriched mantle source was suggested for MBPC gabbros (Deevsalar et al. 2017), M′: depleted asthenospheric source. (c) Trace element modelling of melting, mixing and fractional crystallization. The parameters used in this model are in Supplementary Item 3, Table S2 and S3. The results of melting (calculated in three modes) and mixing event in the source region, and fractional crystallization model in crustal level are given in Table 5. Normalising values are from Sun & McDonough (1989). The mixing equation is from Langmuir *et al.* (1978).

Fig. 10 (a) Schematic representation of the proposed geodynamic scenario for emplacement of within-plate type igneous rocks in the SaSiZ and the UDMA during the Late Eocene. The model involves roll-back of the Mesopotamia slab, combined with detachment beneath the SaSiZ. Next, subduction of the Zagros slab removes the last remaining Neo-Tethys lithosphere between Iran and Arabia and shifts the locus of renewed arc magmatism east to the UDMA. Modified after Zhang *et al.* (in press). The location of the MBPC and Piranshahr (Pi) are shown in Fig. 1b. (b) Summary of the present-day location of the two slab remnants from Neo-Tethyan subduction beneath Iran. Based on seismic tomography results published in van der Meer *et al.* (2018).